ENGINEERING

Large-scale smart bioreactor with fully integrated wireless multivariate sensors and electronics for long-term in situ monitoring of stem cell culture

Jimin Lee[1,2]†, Hojoong Kim[1,2]†, Hyo-Ryoung Lim[3]†, Yun Soung Kim[4]†, Thi Thai Thanh Hoang[5,6], Jeongmoon Choi[5,7], Gun-Jae Jeong[5,8], Hodam Kim[1,2], Robert Herbert[1,2,9], Ira Soltis[1,2], Ka Ram Kim[1,2], Sung Hoon Lee[2,10], Youngjin Kwon[1,2], Yunki Lee[5,6], Young Charles Jang[5,6]*, Woon-Hong Yeo[1,2,11]*

Achieving large-scale, cost-effective, and reproducible manufacturing of stem cells with the existing devices is challenging. Traditional single-use cell-bag bioreactors, limited by their rigid and single-point sensors, struggle with accuracy and scalability for high-quality cell manufacturing. Here, we introduce a smart bioreactor system that enables multi-spatial sensing for real-time, wireless culture monitoring. This scalable system includes a low-profile, label-free thin-film sensor array and electronics integrated with a flexible cell bag, allowing for simultaneous assessment of culture properties such as pH, dissolved oxygen, glucose, and temperature, to receive real-time feedback for up to 30 days. The experimental results show the accurate monitoring of time-dynamic and spatial variations of stem cells and myoblast cells with adjustable carriers from a plastic dish to a 2-liter cell bag. These advances open up the broad applicability of the smart sensing system for large-scale, lower-cost, reproducible, and high-quality engineered cell manufacturing for broad clinical use.

INTRODUCTION

The advent of personalized medicine, propelled by the extraordinary potential of stem cells, is revolutionizing treatment approaches for individuals tackling previously untreatable neurodegenerative and genetic disorders (*1*, *2*). Stem cells, such as primary mesenchymal stem cells, have emerged as formidable therapeutic tools due to their ability to regenerate and exhibit pluripotency (*3*, *4*). However, integrating stem cell–based therapies into mainstream medical practice faces a notable challenge: the lack of a reliable manufacturing platform that ensures consistent production of clinical-grade stem cells while preserving their reproducibility and essential cellular characteristics. While scaling up cell production to meet the increasing demand is feasible, maintaining optimal cell quality throughout the manufacturing process presents a formidable engineering obstacle. One of the primary reasons for this challenge is the absence of continuous monitoring technologies during cell culture (*5*–*7*). Recognizing the criticality of continuous monitoring, biomedical research has consistently emphasized the importance and demand for monitoring cell cultivation (*8*–*13*). As acknowledged by the 2019 Nobel Prize (*14*), oxygen availability affects cell adaptation and response (*15*). Those parameters, such as pH, temperature, and concentration of biochemical analytes, also impact cellular physiology (*16*, *17*). Regrettably, less than 0.5% of experiments conducted between 2014 and 2019 show the measurements of the pH of the culture medium, and none reported dissolved oxygen (DO) levels (*18*). This lack of verification of the culture parameters during experiments compromises the reliability and validity of the outcomes after manufacturing (*19*, *20*). To address this issue, robust standards must be established through proactive monitoring and feedback mechanisms to ensure stable cultivation conditions while enhancing the experimental relevance to in vivo physiology, ultimately improving reproducibility. Recently, single-use cell-bag bioreactors have been widely recognized as an ideal manufacturing platform for generating large quantities of stem cells (*21*–*23*). Although various electrochemical sensors are available (*24*), current monitoring approaches rely on single-point detection sensors that penetrate cell bags, providing only indirect information near the sensors and failing to capture the entire culture environment (*25*). In addition, monitoring the entire cell bag becomes highly challenging as its size increases for scaled production (*26*–*28*). Although many attempts have been made to fabricate sensing systems for in-line monitoring using microfabrication and electrochemical processing techniques, the results are still preliminary and impractical for integration with sensor bags (*29*–*36*). Overall, there is no available solution for real-time, wireless, multi-spatial sensing of cell culture conditions in a cell-bag bioreactor.

Here, this paper reports the development of a large-scale smart bioreactor system with fully integrated wireless multiple membrane sensors and electronics for long-term, continuous, in situ monitoring of stem cell culture. Our technology leverages low-profile, label-free nanomembrane sensors and ultrathin electronics seamlessly integrating with commercial cell bags for in-line culture monitoring

[1]George W. Woodruff School of Mechanical Engineering, College of Engineering, Georgia Institute of Technology, Atlanta, GA 30332, USA. [2]IEN Center for Wearable Intelligent Systems and Healthcare at the Institute for Electronics and Nanotechnology, Georgia Institute of Technology, Atlanta, GA 30332, USA. [3]Major of Human Biocovergence, Division of Smart Healthcare, College of Information Technology and Convergence, Pukyong National University, Busan 48513, Republic of Korea. [4]Biomedical Engineering and Imaging Institute, Department of Radiology, Icahn School of Medicine at Mount Sinai, New York, NY 10029, USA. [5]Department of Orthopaedics, Musculoskeletal Institute, Emory University, Atlanta, GA 30329, USA. [6]Atlanta VA Medical Center, Decatur, GA 30033, USA. [7]Altos Labs-San Diego Institute of Science, San Diego, CA 92121, USA. [8]Institute of Cell and Tissue Engineering, College of Medicine, The Catholic University of Korea, Seoul 06591, Republic of Korea. [9]Department of Mechanical Engineering, Carnegie Mellon University, Pittsburgh, PA 15213 USA. [10]School of Electrical and Computer Engineering, College of Engineering, Georgia Institute of Technology, Atlanta, GA 30332, USA. [11]Parker H. Petit Institute for Bioengineering and Biosciences, Institute for Materials, Institute for Robotics and Intelligent Machines, Georgia Institute of Technology, Atlanta, GA 30332, USA.
*Corresponding author. Email: whyeo@gatech.edu (W.-H.Y.); young.jang@emory.edu (Y.C.J.)
†These authors contributed equally to this work.

and providing real-time feedback. The multifunctional sensor array measures pH, glucose, DO, and temperature with high sensitivity, reliability, and repeatability. Unlike the existing cell-bag sensors, the entire sensor system is soft and flexible, which does not interrupt the cell culture process and natural fluidic motions during rocking motions in a bioreactor. Miniaturized integrated circuits enable the acquisition of wireless, real-time data while capturing spatial information on cell culture qualities within a cell bag. This system provides dynamic, spatially resolved feedback for high-throughput cell manufacturing. Collectively, the comprehensive study of materials, mechanics, manufacturing, and packaging provides the guidelines for developing the advanced sensing platform, which has the potential for deterministic, high-quality manufacturing of therapeutic cells and stem cells for broad clinical and industry use.

RESULTS

System overview of the smart bioreactor with sensors and electronics

The smart bioreactor system includes an array of nanomembrane multifunctional sensors for detecting pH, glucose, DO, and temperature and miniaturized flexible electronic circuits for wireless data monitoring, integrated with a commercially available, single-use, and disposable cell bag (Fig. 1A and movie S1). Using portable devices or

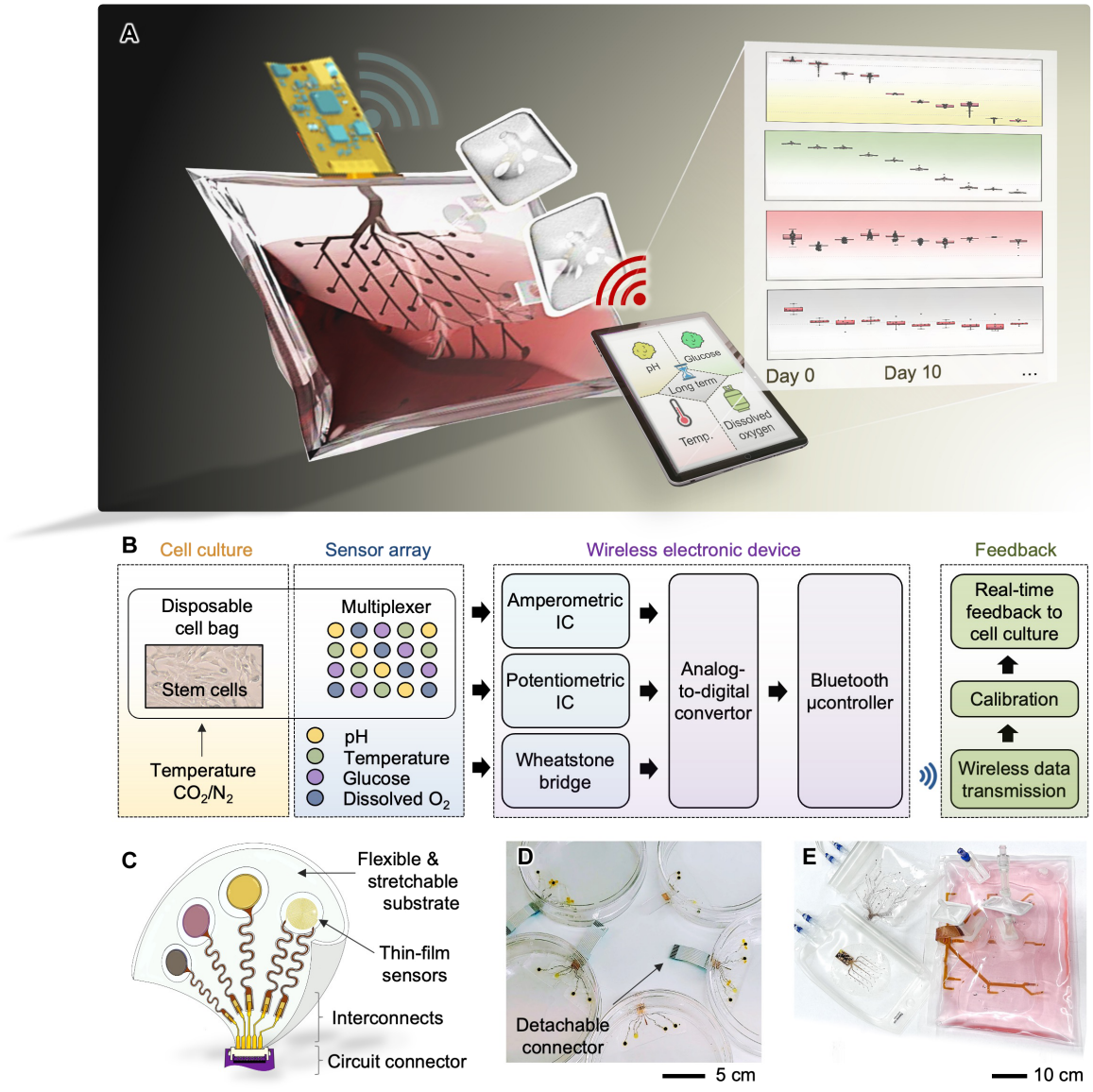

Fig. 1. Overview of a smart bioreactor with integrated multivariate sensors for long-term in situ monitoring of stem cell culture. (**A**) Schematic illustration of a wireless multi-sensing system integrated into a single-use cell bag, which can monitor the cell culture environment in real-time for continuous 30 days. Sensing data are wirelessly transmitted to a mobile device for feedback-based control of culture parameters. (**B**) Flow chart capturing the stem cell culture process using the smart bioreactor system. (**C**) Key features of the multisensory-integrated platform, including soft, thin-film sensors, interconnects, and a circuit connector for a connection with a wireless circuit. (**D** and **E**) Photos showing a completed cell culture platform using a petri dish with the sensor package (D) and a set of different scale cell bags with integrated thin-film sensors for real-time, continuous, in situ monitoring of stem cell culture in a 2-liter volume solution (E).

connecting in-line processing monitors with our system, users can wirelessly receive the in situ stem cell culture information, such as the spatial distribution of cell population and culture areas with non-desirable growth rates or cell states (Table 1). The existing cell-bag sensors are not capable of providing such information to the manufacturers. This multi-sensor system targets detecting stem cell culture with the wireless electronic system (Fig. 1B), providing real-time feedback on culture conditions. Each sensor in the array is interfaced with a unique signal transduction design using amperometric, potentiometric, and Wheatstone bridge circuitry. Once the signals are converted to raw voltages by an analog-to-digital converter (ADC), a microcontroller with the Bluetooth module wirelessly transmits the signals to an external device. The measured signals are calibrated as desired information to realize the condition of the cell culturing and responded to in real time with a sampling rate of 1 Hz, allowing for a collection of a sample per second. The low-profile, thin-film sensor package can be incorporated into any culture platform, including flexible polymer substrates

Table 1. Comparison of different types of cell monitoring systems. hMSCs, human mesenchymal stem cells; iPSCs, human induced pluripotent stem cells; mMSCs, mouse mesenchymal stem cells; C2C12, mouse myoblast cells; mPMs, mouse primary myoblasts; hDFBs, human dermal fibroblasts; HL-1, mouse cardiac muscle cells; CHO, Chinese hamster ovarian cells; MRC-5, human fibroblasts (ATCC CCL-171) cell line; T-47D, human breast cancer cell line; T98G, human tumor cell line; L929, mouse fibroblast cell line; adMSCs, human adipose-derived mesenchymal stem cells; NHDFs, normal human dermal fibroblasts; HaCaT, human immortalized keratinocytes; H1 hESCs, human embryonic stem cells; GM12878, human lymphoblastoid cells; K562, human chronic myelogenous leukemia cells; DO, dissolved oxygen; DCO_2, dissolved carbon dioxides.

Reference	Maximum monitoring time	Sampling rate	Target cell line	Wireless monitoring	System form factor	Sensing parameters	Cell culture platform
This work	30 days	3600 samples/hour	hMSCs, iPSCs, mMSCs, C2C12, and mPMs	Yes (fully integrated)	Array, flexible	pH, DO, temperature, and glucose	Fully adjustable: from culture dish (50 ml) to cell bag (2 liters)
(*79*)	18 days	(Not specified)	hDFBs, hMSCs, C2C12, and HL-1	Yes	Array, rigid	Temperature, pH, impedance, and K^+	Culture dish
(*30*)	11 days	(Not specified)	CHO	No	Single, flexible	Glucose	Cell bag (0.5 liters), culture flask (50 ml)
(*31*)	13 days	(Not specified)	hMSCs	No	Single, flexible	Pressure	Culture flask (0.5 liters)
(*80*)	96 hours	60 samples/20 hours	MRC-5	Yes	Single, rigid	Impedance (cell viability)	Sensor-integrated microbioreactor (<5 ml)
(*32*)	50 hours	(Not specified)	T-47D and T98G	No	Single, rigid	pH and DO	Culture flask (25 cm^2)
(*34*)	2 days	2 samples/6 hours	L929	No	Single, rigid	pH	Culture six-well microplate (~2 ml per well)
(*81*)	3 days	1 sample/24 hours	L929	No	Single, rigid	Glucose	Culture 6-well microplate (~2 ml per well)
(*35*)	134 hours	(Not specified)	T-47D	No	Single, rigid	Temperature and DO	Culture dish (<200 mm^2)
(*36*)	90 min	12 samples/hour	–	Yes	Single, rigid	DO	3D-printed chamber (10 liters)
(*82*)	5 days	(Not specified)	adMSCs, NHDFs, and HaCaT	No	Single, rigid	DO, pH, glucose, and lactate*	Stereolithography 3D-printed bioreactor part (<50 ml)†
(*8*)	3 days	1 sample/8 hours	H1 hESCs, GM12878, and K562	No	Single, rigid	DO and DCO_2‡	T-25 flasks (5 ml) and T-75 flasks (15 ml)
(*33*)	30 hours	10 samples/2000 min (glucose); 5 samples/50 min (osmolality)	–	Yes	Single, rigid	Glucose and osmolality	Plastic chamber

*The dimensions of the prototype bioreactor: 16.5 mm × 45.5 mm. †The commercial optic sensors were mounted in the open-flow microperfusion probe system. ‡The commercial optic sensors repeatedly measured the levels of DO and DCO_2 at 8-hour intervals.

(Fig. 1C). This package has design flexibility in that the number of sensors, an array design, and the placement of sensors could be freely selected upon a target platform or volume of the cell cultivation. A few examples are shown in Fig. 1 (D and E), including sensors in a disposable polystyrene petri dish and different sizes of single-use cell culture bags for bioreactors.

Fabrication of multifunctional thin-film sensors

For cost-effective and scalable manufacturing, we developed a strategy that takes advantage of wafer-scale microfabrication, electrochemical material deposition, and transfer printing of materials (*37*–*39*). We have used microfabrication techniques, allowing wafer-scale manufacturing of solid-state thin-film sensors (Fig. 2A). Through the series of processes, multiple wafers include an array of electrodes with a serpentine line for good stretchability and a solderable contact pad for integration with a sensor interconnect, showing an excellent tear-off characteristic. Depending on the sensor's targeted functions, the multifunctional electrochemical sensors are fabricated by additional deposition of sensing materials and polymer coating. Optical microscope images and illustration in Fig. 2B describe the details of structure layers for offering functions to detect (i) pH, (ii) temperature, (iii) DO, and (iv) glucose. Additional details of the fabrication steps for all sensors, including reference and counter electrodes, and their functionalization process are described in figs. S1 to S6. The pH-detecting sensor was fabricated on the basis of IrO_x membranes deposited via pulsed cyclic voltammetry (fig. S7) (*40*, *41*). A monolayer of IrO_x tends to be easily delaminated and thereby does not ensure long-term stability. At the same time, it is immersed in the solution for 12 hours; thus, Nafion and poly(2-hydroxyethyl methacrylate) (pHEMA) layers were prepared by a combination of drop coating and film curing processes to increase the sensing stability against the culture environment (fig. S8). The thin-film resistive temperature sensor used a patterned Au resistor as the sensing method. The microfabrication process was nearly identical to the sensing platform procedures. Because no physical interaction with the fluid was necessary, the resistor was fully sealed with the top polyimide (PI) except for only two contact pads for electrical connections. The profile for a line thickness is represented in fig. S9, showing the overall thickness under 4 μm. The glucose sensor used PtPdPt nanoparticles on a graphene layer to monitor the glucose concentration in the cell medium by amperometry (*42*, *43*). A PtPdPt nanoparticle–decorated graphene structure was formed on the Au surface by drop casting of graphene-dispersed ink and subsequent electrochemical deposition, while Nafion was deposited by spin coating. Various conjugations of Pt and Pd nanomaterials were used to develop the glucose sensor (fig. S10). The DO sensor used an electron beam–deposited Pt layer incorporated with NiPt nanoparticles (*44*). Although the surface layer of Pt was treated to form nanostructures for increased oxygen sensitivity, the Pt was assumed to be consistently pure in terms of purity because the presence of the nanostructure was negligible. For the transport of gas molecules and surface functionalization, a poly[2-methacryloyloxyethyl phosphorylcholine (MPC)–*co*-*n*–dodecyl methacrylate (DMA)] [poly(MPC-*co*-DMA)] hydrogel was covered at the top of the electrode (*45*). Bottom-row images are the surface morphology of sensing materials of each sensor captured by scanning electron microscopy (Fig. 2B, bottom images). Their cross-sectional views are also shown in fig. S11. These thin-film sensors connect with prepared interconnectors using adhesives and soldering (Fig. 2C). We use the combination of microfabrication and transfer printing to fabricate the film interconnector, consisting of PI-encapsulated Cu traces on a soft elastomer layer. Top PI was patterned to expose only the portions of the bottom Cu layer, allowing individual sensors to be integrated. Various interconnectors were designed and fabricated via microfabrication and laser-micromachining methods to accommodate different types or different volumes of the cell culture platforms (fig. S12). The wireless circuit, connecting the sensor-mounted interconnector, incorporates multiple components (Fig. 2D), such as the Bluetooth-low-energy chip (nRF52, Nordic Semiconductors), front-end signal conditioning (ADS1299, Texas Instruments), amplifier (LM324MX, Texas Instruments), and multiplexers (ADG1606, Analog Devices), to enable acquisition of multiple sensor data as well as wireless, real-time data transmission to a connected mobile device. Equipped with multiplexers, where each multiplexer allows a maximum of eight sensor connections, this device can handle the simultaneous transmission of multiple sensing data from the sensor array. Details of the schematic design for the sensor connection are shown in fig. S13. The wireless circuit can be powered by a lithium-polymer battery (3.7 V) or connected with an USB cable for continuous measurement without the need of charging or discharging the battery. With a charging cable, the use is virtually perpetual. If using the battery with 600-mAh capacity, then the device can record the signals from up to 20 sensor channels over 5 hours. The power consumption of the device is 0.43 W. Figure 2E captures an example of the circuit-integrated cell bag connected to a rocking bioreactor for cell culture. The key features of the smart bioreactor system are highlighted in movie S2.

Performance validation of nanomembrane sensors for detecting pH, temperature, DO, and glucose

Accurate, sensitive, and stable monitoring of cell culture conditions requires that the embedded sensors exhibit consistent sensor-to-sensor characteristics when integrated with bioreactors. In this study, we conducted a series of experiments to validate each sensor's performance, reliability, and long-term usability. Figure 3A shows the four sensors following different sensing principles, including a potentiometric pH sensor, a resistive temperature sensor, and amperometric DO and glucose sensors. Except for the temperature sensor, other sensors require reference electrodes, while the amperometric sensors need the additional use of a counter electrode. The pH sensor measures the potential difference between a reference electrode and a working electrode in a solution. When the sensing electrode comes into contact with a solution with different pH levels, an electrical potential is generated, proportional to the pH level according to the Nernst equation (i.e., −59.2 mV/pH at 25°C) (*46*). Figure 3B summarizes the characteristics of thin-film pH sensors in different pH buffers, verifying a stable reading in the pH range from 4 to 10. This sensor shows an average sensitivity of −57.12 mV/pH, which is near the theoretical value, and it can cover the typical cell culture pH range from 6.5 to 7.8 (*47*, *48*). The long-term pH recording during the 7 days shows the sensor's stability, compared to a commercial sensor (Vernier). The temperature sensor detects temperature changes by measuring the variation in the resistance of the electrode material (*49*). This change in resistance is caused by a temperature-dependent variation in the mobility of charge carriers. In this study, thermally stable Au having a higher thermal conductivity (i.e., 317 W/m·K) as well as a higher temperature coefficient of resistance (i.e., 0.0034/°C) was used as a resistor, enabling to induce a larger and more prompt change in resistance

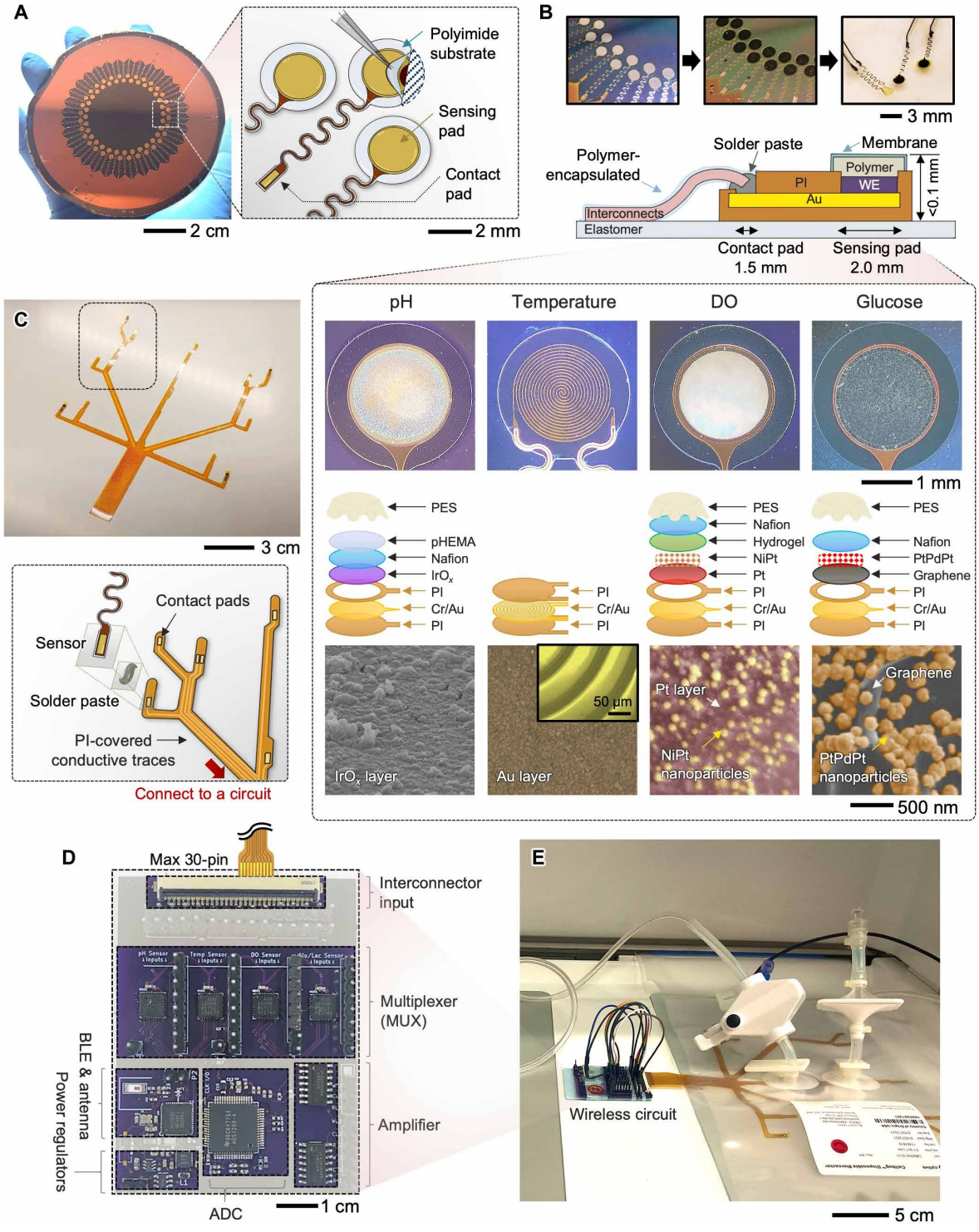

Fig. 2. System architectures of a scalable multi-sensor platform with a wireless circuit. (**A**) Fabrication of an array of thin-film electrodes on a wafer; except for the sensing pad, all areas are fully covered with a polyimide (PI), enabling individual transfer to a different substrate. (**B**) Photos of electrodes before and after electrochemical deposition of active materials (top) and a schematic illustration and photos of the detailed structural design of four sensors (bottom); there are pH, temperature, DO, and glucose sensors with different designs of embedded layers for functionalization. Bottom scanning electron microscopy images show the top surface of each sensor. (**C**) Photos of a fabricated thin-film interconnect layer to integrate four sensors (top) and an exploded drawing of the strategy showing the attachment of each sensor to the interconnector (bottom). (**D**) Top view image of a completed wireless circuit system incorporating multiple functional components [e.g., multiplexer for each sensor, analog-to-digital converter (ADC), Bluetooth low energy (BLE), and antenna] for direct integration with different types of bioreactors. (**E**) Photo of a bioreactor using a single-use cell bag that has a wireless circuit for data acquisition.

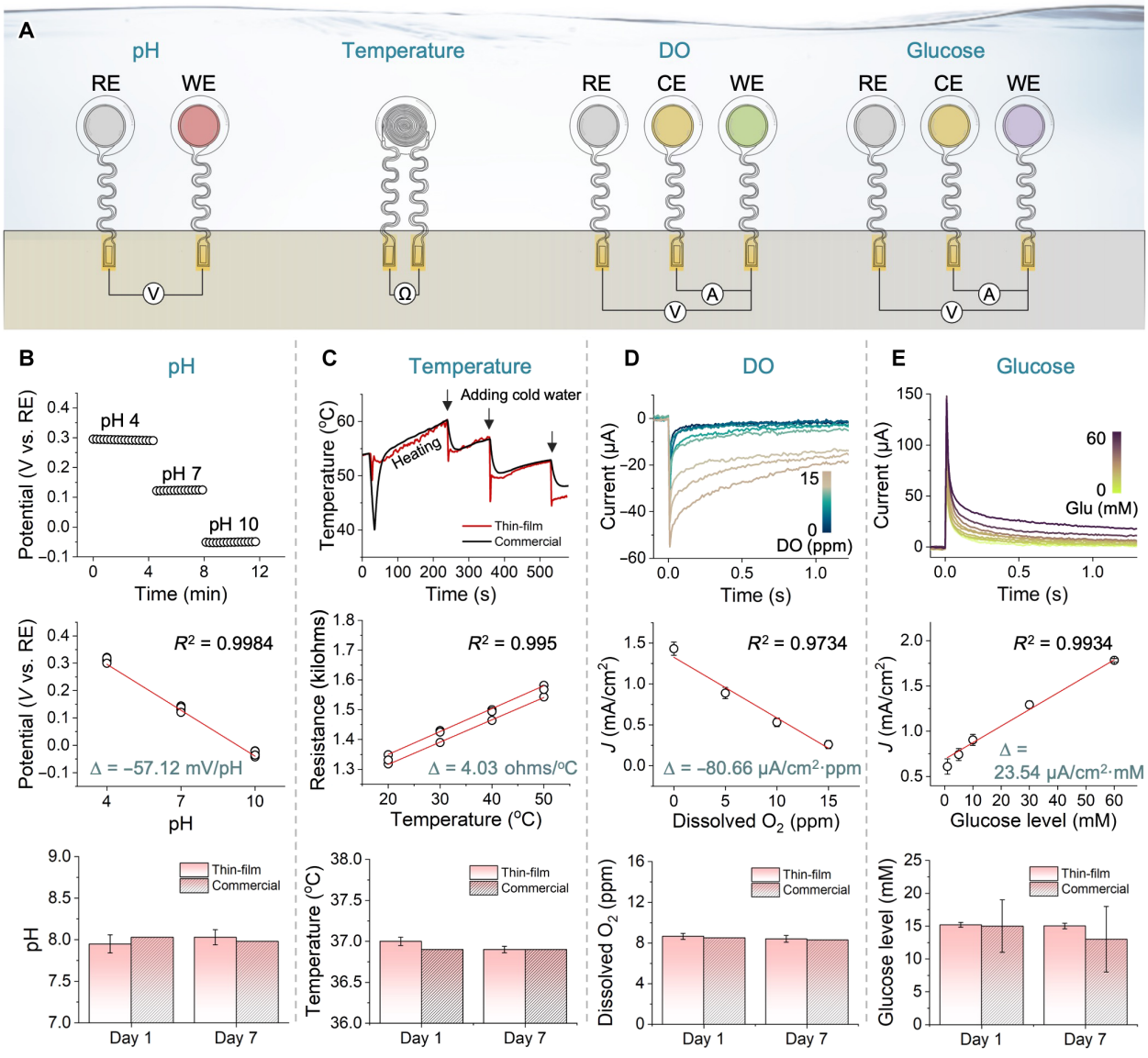

Fig. 3. Performance validation of four sensors in the cell culture monitoring system. (**A**) Schematic illustration showing sensor configurations and working principles of each electrochemical sensor, consisting of reference electrode (RE), working electrode (WE), and counter electrode (CE). Ω, ohms. (**B**) Potentiometric pH sensor performance in different buffers (top), its sensitivity plot (middle; $n = 5$), and stability plot of the thin-film sensor up to 7 days, compared with a commercial sensor (bottom; $n = 3$). *V*, voltage. (**C**) Performance of resistive temperature sensors, showing the comparison with a commercial one (top; the negligible difference between the two sensors), the sensitivity plot (4.03 ohms/°C) (middle; $n = 3$), and the stability plot showing the measurement consistency for 7 days (bottom; $n = 3$). (**D**) Thin-film DO sensor's performance under different DO concentrations from 0 to 15 parts per million (ppm; top), the sensitivity plot of the sensor (middle; $n = 5$), and the 7-day long measurement of DO (bottom; $n = 5$), compared with a commercial oxygen sensor under 8 ppm of O_2. (**E**) Performance of glucose sensors showing the current signal changes in saline with different glucose concentrations from 0 to 60 mM (top), the sensitivity plot of the sensors showing a linearity range to 60 mM (middle; $n = 5$), and the stability plot for 7 days when compared to a commercial one (bottom; $n = 5$). *J*, current density.

upon temperature change (*50*, *51*). Figure 3C shows the experimental results using three temperature sensors. Because of the inherently linear nature of the film resistors' temperature-dependent resistance changes, the fabricated sensors exhibit a uniform sensitivity of 4.03 ohms/°C. The simplicity of the design with full encapsulation contributes to the excellent long-term robustness of the temperature sensors throughout 7 days of monitoring. The DO sensor measures the amount of oxygen in a solution by detecting the current produced by the oxidation at a sensing electrode (*52*). An electrical potential is applied between the reference and working electrodes, and the current produced by the reaction is measured and converted into DO values. The experimental results in Fig. 3D capture the sensor's performance under different oxygen concentrations from 0 to 15 parts per million (ppm) at 22°C. The sensitivity is over −80.66 μA/cm^2·ppm covering a broad DO range of 0 to 15 ppm (*53*). In addition, this sensor shows stable monitoring of DO for 7 days without any introduction of bubbles on the sensor's surface. In contrast, plenty of bubbles were observed on the surface of a

commercial DO sensor (Hamilton Oxysens 120) on day 7, leading to a noise of the sensing signal. Like the DO sensor, the glucose sensor detects the current produced by the oxidation of glucose molecules at a working electrode. The sensor has a working electrode coated with a material that catalyzes glucose oxidation and a reference electrode. An ultrathin, well-stable Ag/AgCl reference electrode is prepared using an electrodeposition technique, including cyclic chlorination. Additional evaluation of the reference electrode is exhibited in fig. S14. Figure 3E shows the current signal variation from a glucose sensor with different glucose concentrations from 0 to 60 mM in phosphate-buffered saline (PBS) clearly showing the different current responses. The sensitivity performance of the sensor shows a linearity range from 2 to 60 mM of glucose concentrations, covering a normal range of cell culture medium (*54*, *55*). The glucose sensor performance for 7 days shows a consistent recording of glucose concentration compared to a commercial sensor (Care Touch). In designing these sensors, we used a transwell membrane to reduce the fouling caused by protein (e.g., direct contact with cells and bacterial infection) and remove mechanical stress on the sensors' surface during cell cultivation. A hydrophilic, low-protein–binding membrane, having submicron small pores, allows for a selective penetration of target materials, such as glucose, oxygen, and proton, while preventing the passage of larger particles such as general mesenchymal stem cells ($D = 15$ to 30 μm) or bacteria. By using customized three-dimensionally (3D) printed molds, we fabricated membranes, as shown in fig. S15. In this study, we tested the effect of different membranes, including cellulose acetate, polyethersulfone (PES), polyvinylidene fluoride, polycarbonate, and polytetrafluoroethylene, on a potential change to optimize the sensor stability (fig. S16). The physical characteristic profiles of the membranes are listed in table S2. Among them, the PES membrane shows the best stability. Thus, this membrane is adapted on the top of the surface electrode and protects the sensor from cells or any contaminants' penetration (fig. S17).

Computational modeling results and sensor's long-term stability and reliability

In this study, we conduct a series of computational and experimental research to validate the system's mechanical stability and reliability for long-term use with rocking bioreactors. Finite element analysis (FEA) is a computational study for determining the optimal design layouts and materials to develop electronic systems (*56*, *57*). Four sensors developed in this work have different thicknesses of PI. The FEA results shown in Fig. 4A capture that the minimum bending radius at any PI thickness up to 10 μm is enough to endure the fluidic fluctuation stress in a cell bag. With PI's thickness set at 2 μm, no damage is identified over 432,000 cycles of continuous bending of the sensor. The onset of fatigue failure is observed at the maximum cycles of 5,863,761. Details of simulation parameters are described in Materials and Methods. Additional studies on the stretchability of serpentine connectors in Fig. 4B show the maximum elongation of ~139% before degradation in the PI-encapsulated Cu trace. The FEA study also helps to determine the optimal combination of functional materials' layers in the sensors developed for cell culture. As a result, Fig. 4C shows the required minimum bending radius for pH, DO, and glucose sensors. For the pH sensor with each x-y coordinate (e.g., a combination of pHEMA and IrO_x), a minimum bending radius determined by the observation of maximum strain is assigned as the z coordinate. The resulting 3D surface plot shows the general trend in flexibility. The thinner pHEMA and IrO_x membranes allow for smaller bending radii, implying higher flexibility. Thickness combination of <100 μm and <16 μm is selected for pHEMA and IrO_x, respectively, to secure effective membrane functionality, showing that a total of 1,498,110 bending cycles could be achieved before a fatigue failure is observed. In addition, the FEA results between hydrogel (within a range of 0 to 100 μm) and Pt (0 to 3 μm) for the DO sensor and between Nafion (0 to 30 μm) and PtPdPt-graphene (0 to 100 μm) for the glucose sensor show that any thickness combination should yield a favorable result with the entire curve positioned below 1 mm in the z plane. The computational analysis indicates the film sensors can withstand the repeated bending caused by continuous rocking motion during the cell culturing process in the bioreactor. The additional FEA datasets, including the temperature sensor and other reference electrodes, are shown in tables S3 to S7. The experimental results in Fig. 4 (D to F) validate the computational study of mechanical stability with a rocking bioreactor system. To ensure both structural and functional reliability, the sensor-integrated system is placed on a rocking module in an incubator (Fig. 4D). For a long-term, continuous test, the sensor-integrated culture dish is filled with cell-free medium at the same temperature without gas control. The sensing outcomes are detected by a mobile tablet, connected by Bluetooth for up to 30 days. The demonstration of wireless, real-time, and continuous data monitoring upon a change in injected solutions is shown in movie S3. Figure 4E shows the received signal strength indicator and Bluetooth data rate detected from the connected device. Both data represent stable wireless connectivity under continuous rocking for consecutive 7 days. Optical microscope and electron microscope images of the four sensors obtained at the start and the end of the 7 days indicate negligible change even at the microscale when comparing the two sets of images (fig. S18). The top row graphs of Fig. 4F show the electrical reliability of the four membrane sensors, evaluated for 30 days under continuous rocking in a cell-free medium. All sensors maintain long-term robustness within 1% of performance variation for 30 days of measurement. The measured sensitivity of the four sensors (bottom row graphs) also shows negligible changes throughout the entire period, which validates reliable performance for cell culturing using a cell-bag bioreactor under rocking motion (fig. S19). In this cell monitoring system, an Android app that we developed offers signal processing with built-in two-point calibration functionality. The main features of the app and the calibration process are depicted in figs. S20 and S21, respectively. To investigate the levels of electricity interference and noise that could arise during real-time wireless data collection, we measured signals by moving the electronic device to various locations (e.g., inside the bioreactor, near the socket, and on the table), as shown in fig. S22. Except for the area close to the socket, the noise effects caused by such interference were negligible. Similarly, to determine the noise level that could arise from the rocking motion of the bioreactor, signal measurements were performed by changing the rpm level (e.g., 2 to 18 rpm) and angle (e.g., 2° to 12°). The optimal conditions for performing the rocking motion were determined to be 10 rpm and 3°, which could effectively ignore the noise level (fig. S23).

Engineering of gelatin hydrogel carriers for 3D cell culture in a bioreactor system

Previously, 2D culture methods have been widely used as the standard technique for stem cells (*58*). However, this cell culture condition

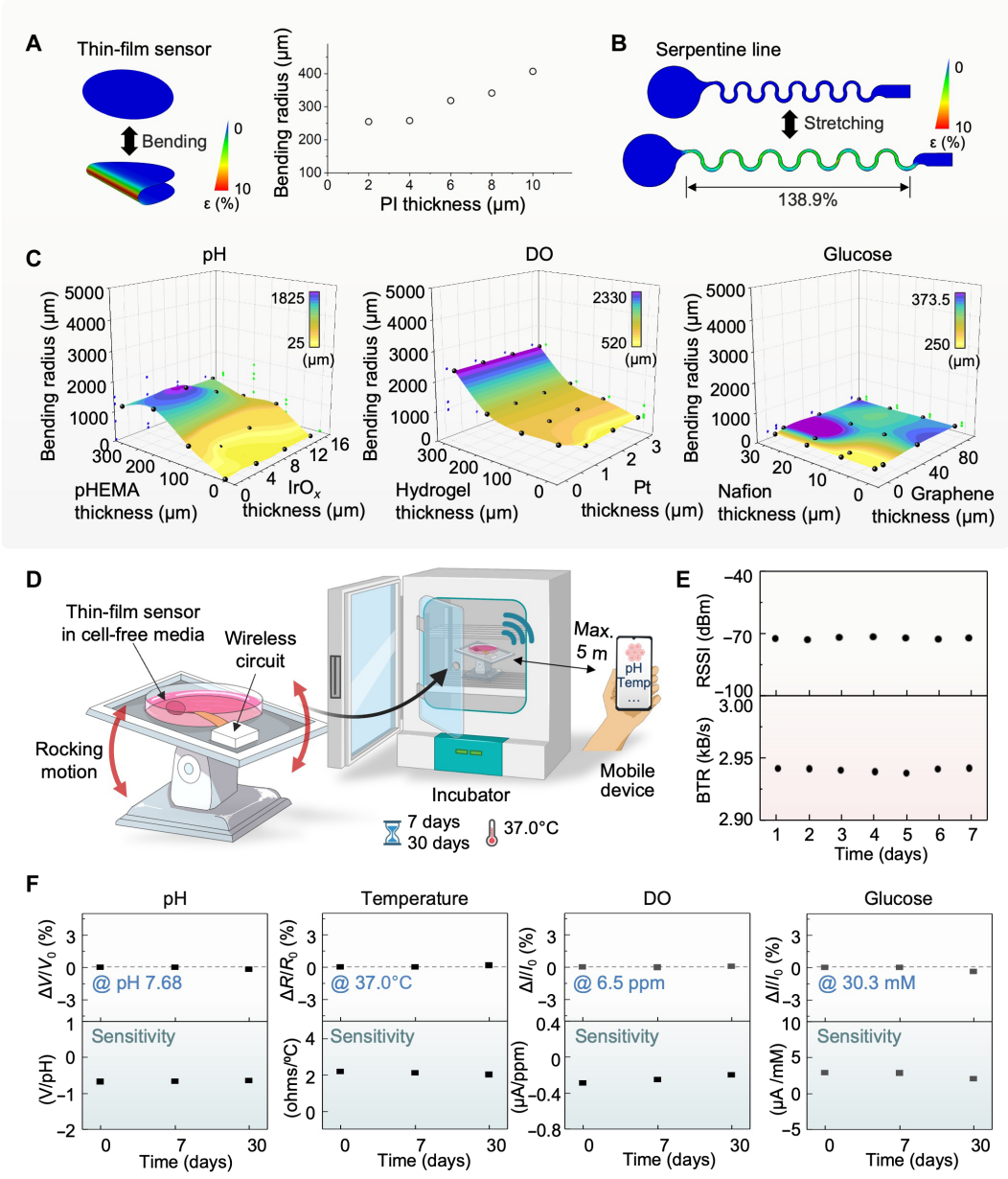

Fig. 4. Computational modeling results and sensor's long-term stability and reliability. (**A**) Bending stability simulation showing the minimum bending radius of a sensor's film according to the covered PI thickness. (**B**) Maximum stretching simulation of a stretchable serpentine line for each sensor's design. (**C**) Surface plot based on minimum bending radii at a given combination of variable membrane thicknesses for three sensors. No film damage at any combination under 10-mm radius is observed over 55,000 bending cycles. (**D**) Schematic illustration of the bioreactor setup to identify long-term sensor reliability with a rocking condition of the bioreactor. The rocking bioreactor is located inside the incubator for up to 30 days. (**E**) Signal strength from the sensor during 7 days of the rocking process, showing the received signal strength indicator (RSSI) and data transfer rate (BTR) at a 5 m distance between the system and the mobile device. (**F**) Reliability of the thin-film pH, temperature, DO, and glucose sensors, evaluated until 30 days under continuous system rocking. All sensors maintain long-term robustness within 1% of performance variation for 30 days.

cannot provide a physiologically relevant microenvironment, which affects cellular activities and functions (*59*). Culturing cells on plastic and glass surfaces often exhibit aberrant behaviors, such as flattened morphology, abnormal polarization, changed response to therapeutic agents, and loss of differentiated phenotype (*58*, *60*–*62*). Thus, for 3D cell cultivation, this study uses cell-laden hydrogels as a scaffold for cell culture in a bioreactor (Fig. 5). Specifically, we developed biocompatible gelatin hydrogels (GHs; GH) that were formed by in situ cross-linking reaction using horseradish peroxidase (HRP) and H_2O_2 (*63*–*65*). The hydrogels have been extensively leveraged as tissue engineering scaffolds because they can provide a microenvironment that mimics the biophysical and biochemical properties of in vivo conditions (*58*, *59*, *66*). Within 3D GH hydrogels (Fig. 5A), target stem cells are encapsulated in combination with a bioreactor for improved culture quality due to the synergistic effects of 3D matrices, dynamic conditions, and accurately controlled parameters (*67*). The cylindrical GH hydrogel

(Fig. 5B) has a porous structure for cell attachment on the surface (2D) or cell encapsulation (3D) with precise control of shape and size (550 μm in diameter and 400 μm in height). With the optimal GH scaffolds, human mesenchymal stem cells (hMSCs) can survive and proliferate without any cytotoxic effects in the static 3D in vitro culture (*67*). The experimental results in Fig. 5C show mechanical properties and in vitro proteolytic degradation behaviors of GH hydrogels that are formed with different H_2O_2 concentrations, ranging from 0.42 mM (indicated as GH-L) to 1.31 mM (indicated as GH-H). The elastic (G') and viscous (G'') moduli of the GH hydrogels are highly controllable and these values are comparable to the elasticity of native tissues. Furthermore, the GH hydrogels exhibit controllable biodegradable properties in the presence of collagenase, the secretory enzyme from the cells for cell proliferation and migration during tissue remodeling. To produce a favorable condition for the cell culture, the mechanical and biodegradable properties of hydrogels have been optimized in this study. Two experimental setups in Fig. 5D validate the performance of 3D stem cell cultivation with a wave bioreactor, providing rocking motions for cell growth. In this study, cylindrical GH hydrogels containing hMSCs were fabricated and transferred to a 50-ml culture plate as a control group and a 1-liter gas-permeable bag as an experimental group. Afterward, the culture plate was incubated in a regular

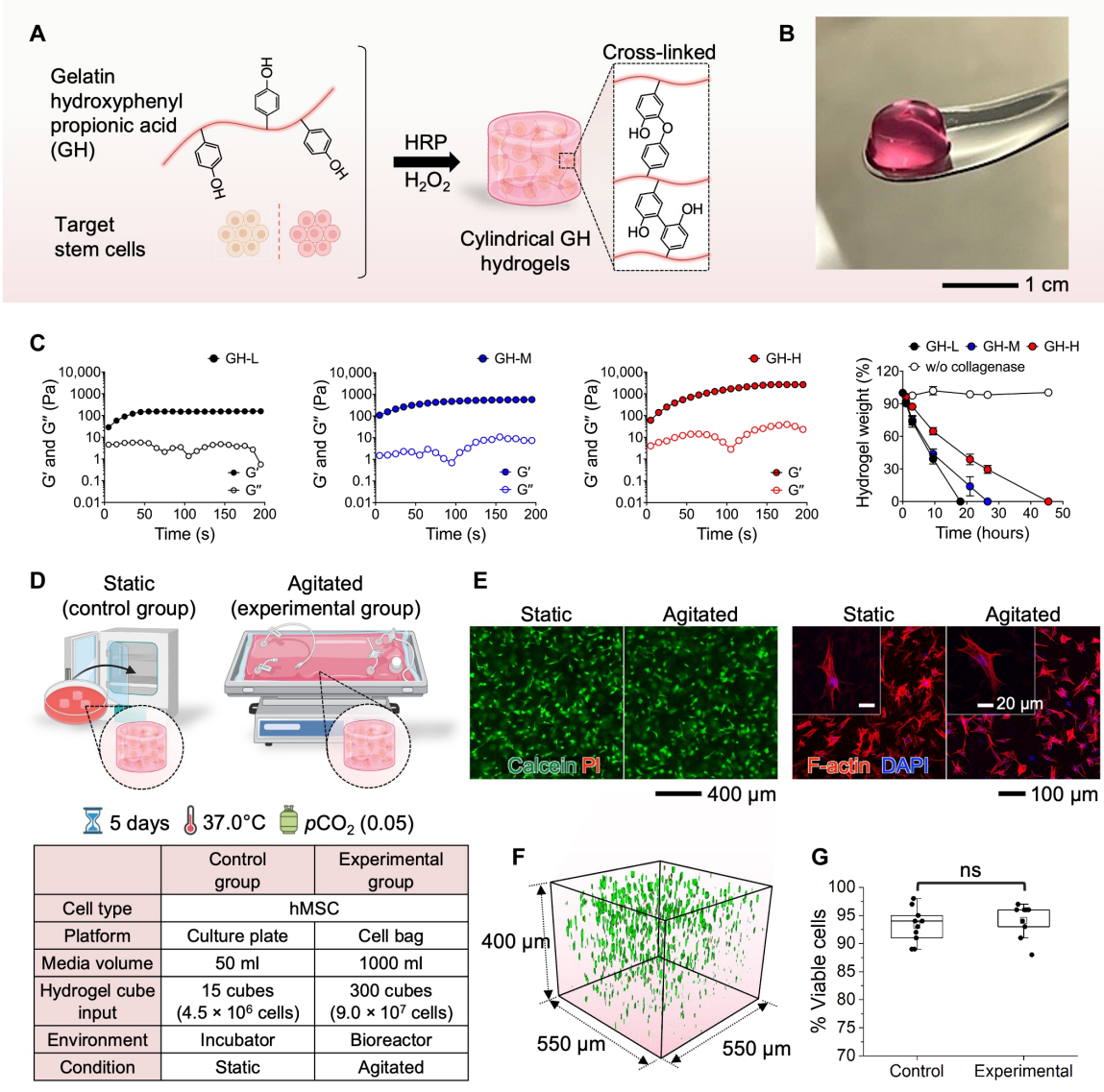

	Control group	Experimental group
Cell type	hMSC	
Platform	Culture plate	Cell bag
Media volume	50 ml	1000 ml
Hydrogel cube input	15 cubes (4.5×10^6 cells)	300 cubes (9.0×10^7 cells)
Environment	Incubator	Bioreactor
Condition	Static	Agitated

Fig. 5. Engineering of GH carriers for 3D cell culture in a bioreactor system. (**A** and **B**) Schematic illustration and a photo of cell-laden gelatin-hydroxyphenyl propionic acid (GH) hydrogel carrier formed by enzyme-mediated cross-linking reaction for stem cell culture with a bioreactor [horseradish peroxidase (HRP)]. (**C**) Mechanical properties and in vitro proteolytic degradation behaviors of the GH hydrogel formed by different H_2O_2 concentrations [0.42 to 1.31 mM; labeled as GH-L (low H_2O_2), GH-M (medium H_2O_2), and GH-H (high H_2O_2)]. G' and G'' represent elastic and viscous moduli, respectively. (**D**) Experimental design for 3D hMSCs culture in the conventional incubator (left; static control group) and the rocking bioreactor (right; agitated experimental group). The detailed conditions are in the table below. (**E**) Fluorescence images showing the high viability of the harvested hMSCs (left) and cell morphology (right) images of the cultured cells. DAPI, 4′,6-diamidino-2-phenylindole. (**F**) Cell distribution shown in the GH hydrogel. (**G**) Comparison of cell viability in the GH hydrogels cultured in the control (incubator) and experimental (bioreactor) [not significant (ns)].

incubator at 37°C, 5% CO_2, and 95% humidity while the bag was placed on a rocker for homogenous mixing of the medium. External conditions, including temperature and CO_2 concentration, were kept constant. On day 5, the hMSC-laden GH hydrogels were collected, and the cells were stained with calcein-AM/ethidium homodimer-1 (EthD-1) and Phalloidin-iFluor 647/Hoechst reagent to assess cell viability and morphology. The images in Fig. 5E show the results of live/dead staining and cell morphology of the cultured hMSCs. In both static and agitated conditions, most cells are viable. Green color–stained live cells have been observed with homogeneous distribution within the hydrogel matrix, exhibiting >93% cell viability (Fig. 5, F and G). Both conditions exhibit well-elongated 3D cell spreading for cell proliferation. That is, there is no distinct difference between the harvested hMSCs that are not exposed to mechanical stimulation and the ones that are exposed to continuous rocking via the bioreactor. The time-course morphological changes and cellular growth of hMSCs harvested in GH hydrogels under agitation are summarized in fig. S24. The hMSC cells inside the hydrogels underwent morphological changes, transitioning from a round shape on day 1 to a spindle shape on day 5. Concurrently, the number of living cells increased, as evidenced by the cell counting kit–8 (CCK-8) assay. The threefold higher optical density (OD) from day 1 to day 5 indicates an increase in cell number. To substantiate the efficacy of 3D hydrogels in providing optimal cellular environments, we used a methodology to create 2D disk-shaped hydrogels. Using the same method, we encapsulated hMSC cells and fostered their growth for a duration of 5 days. The summarized results in fig. S25 demonstrate the notable development of elongated protrusions at the cell peripheries within the 3D hydrogel matrix. This observation underscores the capability of 3D hydrogels to establish stable and conducive conditions for cellular cultivation. Consequently, we successfully demonstrated the superiority of using 3D hydrogels within a bioreactor for in vivo cell cultivation.

Monitoring human iPSC culture with bioreactor systems

Human induced pluripotent stem cells (iPSCs) can be obtained through the reprogramming of differentiated human cells (*68*). The generation of iPSCs addresses the limitations associated with embryonic stem cells, particularly those related to ethical concerns. Using iPSCs, researchers can create various disease models for regenerative medicine and cultivate liver cells, neurons, or other cell types to engineer personalized therapy models (*69*). Consequently, the production of iPSCs becomes a primary requirement for further studies. Monitoring parameters during iPSC production can enhance cell production efficiency and assist in scaling up production because we can maintain optimal conditions for cell growth through precise parameter control. On the first day of iPSC culture, small colonies adhered to the Matrigel-coated dish with a diameter of 100 to 200 μm (fig. S26). After 2 days of biosensor installation, the iPSC colonies continued to grow and expanded by more than threefold. The colonies were compact with well-defined edges, and all cells exhibited a high nucleus/cytoplasm ratio, which indicated the right morphology of iPSCs with no differentiation (*70*). On day 4, iPSCs exhibited robust growth, reaching over 80% confluency, indicating that they were ready for passage and storage. The morphology, confluency, and time required to reach full confluency of iPSCs with biosensors installed were similar to control iPSCs. This suggests that biosensors had no discernible effect on iPSC culture. The monitoring results of iPSC cultivation over a 5-day period are fully documented in fig. S27. Four different types of sensors (pH, temperature, DO, and glucose) were arranged in four sets and placed in the culture dish. The medium solution was exchanged every other day. On day 5, a notable drop in pH, glucose, and DO was observed, indicating a potential contamination issue starting from the sensor 4 areas.

Monitoring mPM proliferation and differentiation with bioreactor systems

Primary cells are mature cells harvested from a specific tissue type. The main advantage of using primary cells in tissue engineering strategies is their potential for immunological compatibility. In experimental models for pathological studies, another advantage is that they retain functions and phenotypes closely resembling those in in vivo organs. However, challenges such as limited lifespan, density, rapid phenotypic changes, availability, and inter-donor variability impede their progress in applications. To address these limitations, in vitro primary cell culture, precisely controlling the variables defining the microenvironment, is considered an important procedure to minimize cellular changes. In this study, we cultured mouse primary myoblasts (mPMs) isolated from Pax7/TdTomato mice and applied biosensors to monitor various parameters regarding cell culture conditions. The experimental setup in Fig. 6A shows cell culture dishes in an incubator for static mPM cultivation to validate the stability. After mPMs were attached to a Matrigel-coated dish, four biosensors were installed, similar to the setup shown in fig. S27. Within 2 days, the myoblasts proliferated, enhancing cell density and reaching ~80% confluency (Fig. 6B). Subsequently, the media were switched to differentiation media. The mPMs underwent differentiation, migration, and fusion to form myotubes. Furthermore, myoblasts and myotubes continuously fused, resulting in the formation of larger myotubes by day 4. In addition, myotubes exhibited the ability to fuse with each other. No notable differences were observed between mPMs with and without biosensor installation (fig. S28). Figure 6C displays the fully recorded data during mPM culture using different cell medium solutions for proliferation and differentiation, respectively. An intriguing result was observed in the pH variation during cell differentiation; the four pH sensors, separated from each other by a minimum distance of 3 cm, recorded a marked change in pH values ranging from 7.0 to 7.8. However, the occurrence of reaching the lowest pH for each sensor happened at different time points, emphasizing the importance of local monitoring related to regional information. Meanwhile, the commercial pH sensing electrode was unable to capture the precise variation.

Demonstration of GH-encapsulated cell culture with bioreactor systems

This study focuses on demonstrating GH-encapsulated stem cell culture with two different systems. The sensor-integrated system in the culture dishes could offer wireless, real-time, continuous monitoring of C2C12 cells for 6 days (fig. S29). Photos in fig. S29A reveal increased cell count and elongated cell morphology in the medium for 6 days. The details of experimental results in cell culture in-line monitoring appear in fig. S29B, showing two datasets: one without cells and the other with cells. Consistent with mammalian cell culture, the measured pH and glucose levels exhibit a downward trend due to the acidification and deoxygenation of the culture medium caused by cellular metabolism (*8*). In terms of performance validation of four sensors, our nanomembrane wireless electronic system shows excellent agreement with the point-measurable commercial sensors, regardless of the presence or absence of cells in the

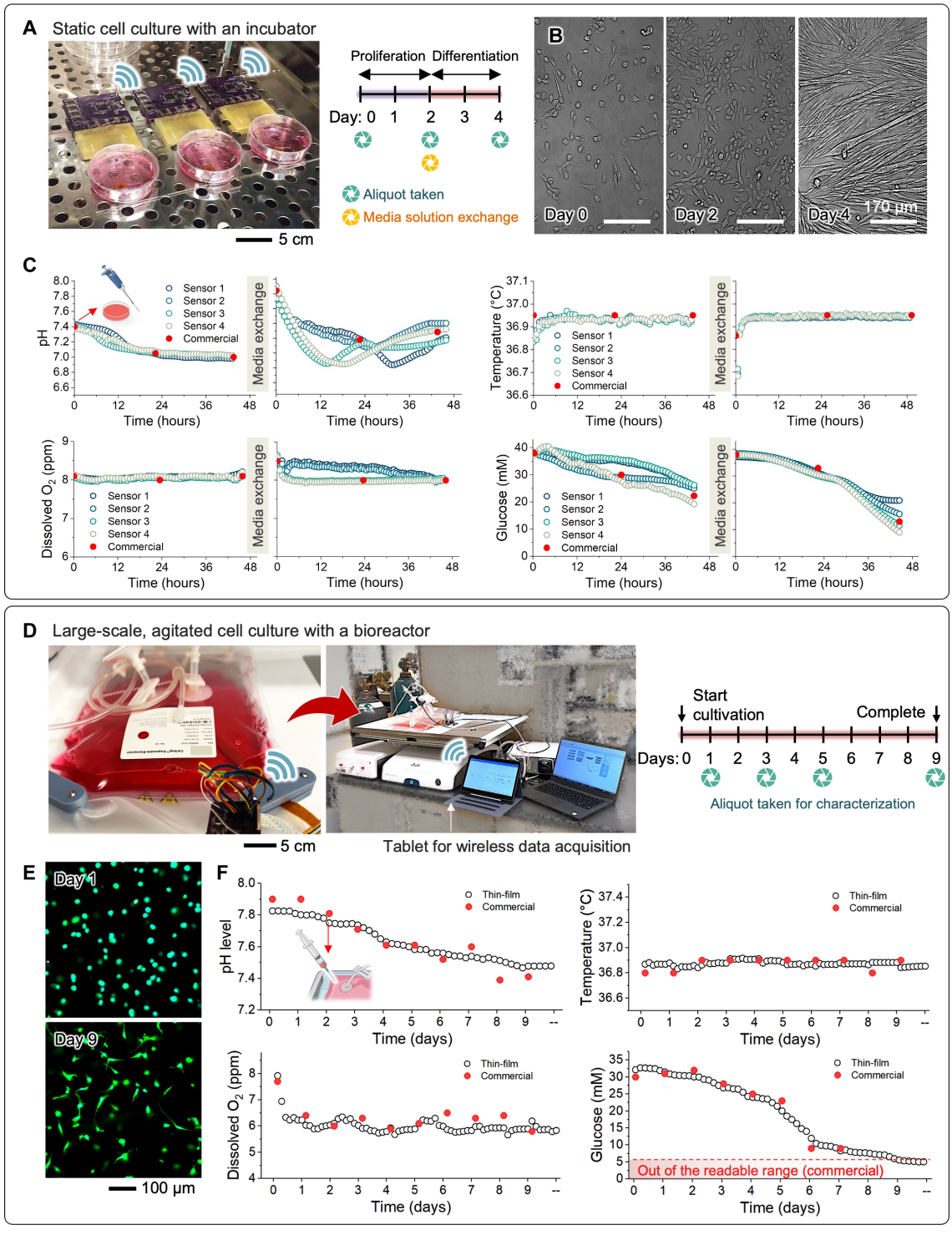

Fig. 6. Demonstration of cell culture with two representative systems. (**A**) Static culture of mouse primary myoblasts (mPMs) within a conventional incubator. (**B**) Representative optical images of mPMs, showing progressive cellular growth (day 2) and subsequent differentiation (day 4) over time. (**C**) Monitoring results, including pH changes, temperature variations, and levels of the DO and glucose in the cell medium over time. The red-filled circles in all graphs represent the measured values obtained using a commercial sensor or laboratory sensor. (**D** to **F**) Large-scale, agitated, GH-encapsulated stem cell culture with a bioreactor. (D) Photo of the flexible sensor-integrated 2-liter cell bag with a rigid prototype of wireless circuit, along with the experimental conditions for hMSC culture in hydrogels within the bioreactor. (E) Representative cell morphology cultured for 9 days in the bioreactor. (F) Monitoring results for a continuous period of 9 days. The red-filled circles in all graphs represent the measured values obtained using a commercial sensor or laboratory sensor.

medium. Unlike the discrete data recording of the conventional sensors, the all-in-one smart system offers wireless, continuous, real-time monitoring of the in-line culture process inside an incubator without the need for multiple sensors and separate data acquisition tools. In addition, our system avoids the risk of contamination and adverse outcomes from temperature fluctuations and inadequate oxygen supply during the incubator opening for cell collection or pH measurements. The data in fig. S29 present the monitored data in an environment containing only cell culture medium without cells, showing a highly constant and continuous progression compared to the data points obtained from commercial sensors. Furthermore, our study shows the successful monitoring of cell growth in mouse MSC (mMSC) culture using a continuous rocking module (fig. S30). As the culture time progressed, the bioreactor system maintained precise control over temperature and DO levels, while the pH and glucose values decreased by up to 50% compared to their initial values, indicating the proliferation of mMSCs within the cell bag. A sensor-integrated wave bioreactor system demonstrates a large-scale, long-term in situ monitoring of stem cells (Fig. 6D). This study uses human MSCs and monitors the culture processes over 9 days under continuous rocking motions. A commercial 2-liter single-use cell bag integrates the membrane sensors and electronics (fig. S31). An example of the real-time data acquisition of pH, glucose, DO, and temperature values appears in movies S1 and S2 with the bioreactor system. The results in Fig. 6E show the viability of hMSCs through the live/dead cell staining assay of aliquots containing cell-laden GH hydrogels (see fig. S32 showing each channel separately). This excellent cell viability (>95%) proves that the sensor-integrated platform is fully biocompatible and capable of continuously monitoring all parameters without any cytotoxic effects. In addition, compared to cell morphology on day 0, the hMSCs cultured over 9 days exhibit a highly stretchable morphology, indicating favorable cellular growth. The ability of the stem cells to increase over time confirms the favorable culture conditions provided by our system. This result substantiates the effectiveness and reliability of the all-in-one system in delivering stable and continuous monitoring results (Fig. 6F). Similar to the other cell culture, successful cellular metabolism led to the acidification and deoxygenation of the culture medium, as evidenced by the consistent drop in pH and glucose levels. During the culture, medium samples were collected daily through the harvest line on the cell bag and measured using commercial probes to compare the device's performance, which introduced slight fluctuations in temperature, pH, and DO readings. The multivariate sensor platform can be tailored to adapt to large-scale cell culture by incorporating up to eight active sensors per representative working electrode. The experimental results in fig. S33 display the hMSC cultivation obtained from two sensor arrays. Sensor array #1 was placed in the middle of the cell bag, while sensor array #2 was integrated near the edge of the bag. These results show consistent trends but slight spatial differences, indicating the potential of this multivariate sensor array to provide accurate spatial information on cell distribution and identification of areas with abnormal pH or temperature conditions. Collectively, this research presents the first demonstration of a large-scale smart bioreactor with fully integrated wireless multi-sensors and electronics for long-term in situ monitoring of stem cell culture. Compared to prior work (Table 1), this system's key advantages are a high data sample rate, integrated wireless sensors, 30-day-long monitoring, and scalability to cover from culture dishes to 2-liter cell bags. By using flexible and multivariate sensor arrays, our platform achieves real-time and continuous monitoring of cellular demands, capturing both temporal and spatial variations in culture conditions. This advancement in high-throughput cell manufacturing enables precise adjustment of nutrient feeding strategies and optimization of bioreactor conditions, ultimately leading to improved cell density, enhanced productivity, and large-scale cell manufacturing.

DISCUSSION

The smart bioreactor system presented here demonstrates a promising route toward scalable, low-cost, and feedback-enabled cell manufacturing in both clinical and research settings. The fully integrated sensors and electronics with a rocking bioreactor show the accurate, wireless, and real-time monitoring of pH, temperature, DO, and glucose with different types of cells, including iPSCs, mPMs, C2C12, hMSC, and mMSC. This system enables continuous assessment of spatial and temporal changes in the culture environment, providing concurrent feedback and active management capabilities for high-throughput cell manufacturing. The nanomembrane set of flexible electrochemical and electrical sensors shows excellent sensitivity with a smaller sensor size than rigid commercial-use sensors. The experimental study, conducted under a continuous rocking motion for 30 days, validates the device's structural integrity, longevity, and reliability of the flexible wireless sensors, showing a sensitivity change of less than 1% during the time span. With GH carriers, our system demonstrates the accuracy, reproducibility, and scalability of stem cell culture with a 2-liter cell-bag bioreactor system. In addition, our biosensors can precisely monitor pH, temperature, DO, and glucose in the cell medium in situ, overcoming the limitations of standard cell cultures. Cells grow at different rates, making it challenging to understand the day-to-day occurrences of changes in the culture medium (*8*). Therefore, precisely controlling these parameters can enhance the reproducibility of in vitro cell culture and accurately recapitulate physiological conditions, especially for sensitive cells such as iPSCs or primary cells. Maintaining stable parameters provides a greater opportunity to establish the relevance of experimental results in various biomedical research contexts. Future work will focus on the engineering development of additional in-line process monitoring sensors and validate the system's scalability with larger cell bags and multiple bioreactor platforms for deterministic, high-quality manufacturing of therapeutic cells and stem cells for broad clinical and industry use.

MATERIALS AND METHODS

Fabrication of pH sensors

A conventional microfabrication process was used to fabricate flexible, film-type pH-sensing electrodes. The pH-sensing electrode was selectively functionalized through electrodeposition within a three-electrode configuration. This setup included a commercial Ag/AgCl reference electrode, a counter electrode made from platinized titanium mesh, and the crafted gold (Au) electrode, which was linked to an electrochemical workstation. The sensing component of the pH sensor was coated with iridium oxide (IrO_x) by electrodeposition. The electrodeposition solution comprised 4.5 mM iridium tetrachloride ($IrCl_4$; Thermo Fisher Scientific), 130 mM hydrogen peroxide (H_2O_2; Merck), and 40 mM oxalic acid dihydrate ($C_2H_2O_4{\cdot}2H_2O$; Sigma-Aldrich), with the pH adjusted to 10.5

using anhydrous potassium carbonate (K_2CO_3; Sigma-Aldrich). The mixture was stored in a dark amber bottle at room temperature for 2 days to ensure stability before being refrigerated at ~4°C until further use. The Au working electrode was submerged in this solution, and a pulse potential (0.7 V for 2-s on, followed by 0.0 V for 10-s off) was applied against the commercial Ag/AgCl electrode for a total of 300 pulses. Upon formation of the IrO_x pH-sensitive layer, a coating of 2.5% Nafion (Sigma-Aldrich) and pHEMA membranes was applied to improve biocompatibility and extend the operational life of the sensor. The pHEMA precursor solution was prepared with 2-hydroxyethyl methacrylate (Sigma-Aldrich), ethylene glycol dimethacrylate (Sigma-Aldrich), 1-dodecanol (Sigma-Aldrich), and 2,2′-azobis(2-methylpropionitrile) (Sigma-Aldrich). The membrane was subsequently cured thermally at 130°C for 10 min. The finalized film sensor was affixed to a flexible substrate (e.g., PDMS), and an electrical wire was connected by soldering. To protect the connection yet expose the sensor surface to the analyte solutions, the connection point was encapsulated with PDMS. Additional fabrication details and illustrations are provided in fig. S1.

Fabrication of temperature sensors

The thin-film temperature sensor was fabricated using a photolithographically patterned Au resistor, following a microfabrication process similar to that used for the electrochemical sensors. Initially, a composite layer of polydimethylsiloxane (PDMS)/PI was spin-coated onto a 100-mm silicon wafer to form a substrate. Subsequently, a serpentine-shaped pattern was created for the copper (Cu) layer, which was deposited via sputtering. This was followed by the sequential lamination of chromium (Cr) and Au layers to form the resistive element. After the deposition of the metal layers, the entire structure was encapsulated with an additional layer of PI, which was then patterned to expose only the contact pads required for electrical connections. The patterning of this top PI layer was achieved using a reactive ion etching process that selectively removed the PI material to reveal the underlying contact pads. For clarity and guidance, a schematic representation detailing each step of the temperature sensor's fabrication process is illustrated in fig. S2.

Fabrication of DO sensors

Flexible DO sensors were produced by electrodeposition on a platinum (Pt) layer, followed by the deposition on nickel (Ni) and Pt nanoparticles. Figure S3 presents a schematic diagram illustrating the fabrication process for the DO sensor on flexible Au electrodes. Pt deposition was performed using a dc power supply, set at 0.01 mA/cm^2 for 3 min. The deposition bath contained a precursor solution of 0.035 M chloroplatinic acid hexahydrate ($H_2PtCl_6{\cdot}6H_2O$; Sigma-Aldrich) and 0.5 M sulfuric acid (H_2SO_4; J.T.Baker). Subsequent electrodeposition of Ni/Pt nanoparticles onto the Pt layer used a three-electrode potentiostat, immersing the electrode in the respective precursor solutions. A current density of −3 mA/cm^2 for 5 min was applied for Ni deposition from a plating solution (Sigma-Aldrich), and a potential sweep from −0.4 to 1.0 V at 100 mV/s in three segments was used for Pt deposition against a commercial Ag/AgCl reference electrode. A Nafion layer was then applied to the surface and allowed to air-dry for 30 min. For surface functionalization, a hydrogel consisting of poly(MPC-*co*-DMA) was introduced as a gas-permeable layer.

Fabrication of glucose sensors

A series of glucose sensors were fabricated on graphene sheets with electrodeposited Pt and palladium (Pd) nanoparticles to create a PtPdPt electrocatalyst–based glucose sensor, aimed for use in cell culture environments. Addressing the issues of rapid activity loss in catalytic sensors due to the chemical and oxygen concentration in their environment, an enzyme-free sensor design was pursued to enhance sensing capabilities during cell cultivation. PtPdPt nanoparticles were deposited on graphene sheets, which facilitated the dispersion of the nanocatalysts without aggregation. A dispersion of graphene was prepared by mixing 0.5 wt % graphene flake powder (Sigma-Aldrich) in 200 ml of pure ethanol, followed by extensive ultra-sonification. Each wafer having plenty of Au electrodes was treated with O_2 plasma for ~1 min to render the surface of the Au electrodes more hydrophilic before drop casting the graphene dispersion. For each single Au electrode, 0.5 μm of the graphene solution was applied using a micropipette, and the wafer was then placed on a hot plate set to 60°C to dry completely for 5 min. After the graphene sheets were drop-coated and dried on the Au conductors, nanoparticle formation was achieved via cyclic electrodeposition. Figure S4 delineates the glucose sensor fabrication steps on flexible Au electrodes. Using the three-electrode system described previously, PtPdPt nanoparticles were electrodeposited onto the graphene substrate. The electrode for glucose detection was submerged in a mild sulfuric acid–based solution, applying varying potentials: from −0.4 to 1.2 V over five cycles at 100 mV/s for Pt and from −0.4 to 1.0 V over three cycles at 100 mV/s for Pd, versus a commercial Ag/AgCl electrode. Subsequently, a Nafion layer was added on the top and dried in air for 30 min.

Fabrication of reference and counter electrodes

The reference and counter electrodes were made of the Au electrodes by the same microfabrication process as the other sensors. In addition, silver (Ag) deposition, electrochemical chlorination, and membrane coating were integral in crafting the reference electrodes. An aqueous solution was prepared by mixing 0.02 mM silver nitrate ($AgNO_3$; Sigma-Aldrich) and 1 M potassium nitrate (KNO_3; Sigma-Aldrich). The bare Au electrode was dipped in this prepared solution and subjected to a potentiostatic scan at −0.4 V against a commercial reference electrode for 5 min, leading to the Au deposition. For chlorination, a precursor solution consisting of 0.1 M potassium chloride (KCl; Sigma-Aldrich) and 0.01 M hydrochloric acid (HCl; Sigma-Aldrich) was prepared. The Ag-deposited electrode, once dipped in the diluted HCl solution, underwent cyclic voltammetry, sweeping potentials from 0.1 to 0.4 V over five segments at a scan rate of 50 mV/s. To know the Ag/AgCl surface with voltage stability to different pH, polyvinyl butyral (PVB; Sigma-Aldrich) matrix including KCl was used as a salt bridge. PVB-KCl membrane cocktail was prepared by mixing PVB, KCl, and methanol. After drop coating the cocktail on the Ag/AgCl electrode, the surface was dried overnight. Additional Nafion membrane was added on the surface to avoid leaching of the KCl salts from the surface of the Ag/AgCl/PVB-KCl and dried for 30 min in the air. Figures S5 and S6 show the schematics of the fabrication procedure for the reference and counter electrodes.

Computational analysis

Analysis software (fe-safe, 3DS) in conjunction with ABAQUS is used to inspect for the failure of mechanical bending simulation.

Table S1 lists the materials used in the fabrication of the sensors and their respective properties, such as the allowable thickness range, modulus, and maximum strain (*71*–*78*). Some layers have been assigned with fixed thickness values for problem simplification and to ensure sensor functionality. To reveal the minimum bending radii for the five sensors, model representations are created in the ABAQUS environment. They are bent up to 180° with varying radii until the maximum strain is observed in any layer. If a bending degree larger than 45° is observed, then the particular combination of two materials is considered bendable with the specified bending radius. All data points are marked in the 3D plot space.

Characterization of electrochemical sensors

The electrochemical sensors were subjected to characterization to evaluate their selectivity, sensitivity, and reproducibility. To simplify the circuits, a two-electrode system was used for the potentiometric pH sensor, with Ag/AgCl electrodes serving as both reference and counter electrodes. The pH potential was measured while the sensor was submerged in solutions of different pH levels (such as pH 4, pH 7, pH 10, and PBS solution with pH 7.4) to generate a calibration curve and the performance was compared with the data obtained from a commercial pH sensor (Vernier Go Direct pH sensor). To determine the temperature monitoring calibration curve, the resistance between the two tips of the Au coil, which served as working and reference/counter electrodes, was measured while the solution was heated within a range of 20° to 60°C. To compare with a commercial temperature sensor (Go Direct Temperature Probe, Vernier), two types of sensors were placed in a heated solution at 60°C, and the values from each sensor were monitored as relatively cold solution was added to the warm solution. The current data from the amperometric sensors, specifically the DO and glucose sensors, were recorded under applied voltages of −0.4 and 0.25 V, respectively. Calibration solutions with varying DO levels were prepared by fully purging N_2/O_2 gas mixture, and their numerical values were evaluated using a commercial DO sensor (Hamilton Oxysens 120). Calibration solutions for measuring glucose levels were prepared by dissolving different amounts of D-(+)-glucose powder (99.5%, Sigma-Aldrich) in PBS solution to achieve glucose levels within a range of 1 to 60 mM. The glucose level of every glucose solution is measured by using a commercial sensor (Care Touch). The sensors were characterized using a wired electrochemical analyzer (Interface 1010E, Gamry Instrument) before being operated with the wireless hardware.

Fabrication of a sensor array system

When choosing a culture platform, there are two main options to consider: a petri dish scale platform suitable for volumes under 100 ml and a cell-bag–scale platform designed for volumes exceeding 500 ml. The choice of platform depends on the desired size of the target sensing array. Furthermore, the fabrication method can be selected on the basis of the chosen platform and target array size. Two possible methods include wafer-scale microfabrication, which is a more complex and precise process suitable for smaller arrays, and simple laser cutting, which is a more straightforward and cost-effective option suitable for larger arrays. For the sake of comparison in terms of the platform scale, fig. S12 displays representative photographs of two distinct processes. The rough manufacturing cost of the sensor array, which consists of a total of 36 sensor sites, is presented in table S8, with the material cost being below $0.93 per unit of the device.

Integration of an all-in-one sensing platform

The electrochemical sensors and sensor array were prepared and electrically interconnected via soldering. Subsequently, the active surfaces of all electrodes were covered with 3D structured PES membrane to safeguard against environmental disturbances. To mitigate external interference during the transmission of electrical signals, a curable polymer, such as medical-grade epoxy or PDMS was used to encapsulate the connections. This encapsulation serves to insulate the components from subreactions or side reactions induced by ion diffusion in the cell medium. Once assembled, the integrated sensing platform was transferred to either a cell culture bag or a petri dish. The underside of the sensing platform was coated with medical-grade epoxy to secure it to the substrate. Sterilization of the cell culture bag or petri dish was achieved with a 70% ethanol solution, followed by exposure to ultraviolet (UV) light for a duration exceeding 12 hours to ensure thorough sterilization. Before use, the platform was extensively rinsed with Dulbecco's PBS (DPBS, 1×; Gibco) to remove any residual dust.

Cell-free culture test

To verify the long-term stability and integrity of the sensing platform, a cell-free cultivation was conducted with a continuous rocking motion. The cell-free culture medium was prepared by mixing Dulbecco's modified Eagle's medium (DMEM; Gibco) with 10% fetal bovine serum (FBS; Gibco) and 1% penicillin-streptomycin (PS; Gibco). The integrated sensing platform was submerged in the cell-free culture medium and placed on a uniaxial rocker in an incubator. Mechanical failure, electrical connectivity, and sensor/electronics performance were periodically checked on the 7th and 30th days of continuous rocking. The data were wirelessly transmitted to a mobile device located 5 m away from the incubator. A schematic experimental setup is shown in Fig. 4D.

Preparation of a rocking incubator system

To ensure thorough disinfection of the internal space within the cell bag, a meticulous two-step process was implemented. First, the system underwent a rigorous cleaning procedure involving three rounds of treatment with a 70% ethanol solution. Subsequently, the system was subjected to a 12-hour exposure to UV light. Following UV sterilization, the entire cell bag inside was gently washed with PBS to eliminate any residual traces of ethanol. The cell bag integrated with sensors was affixed to a rocking bioreactor system (WAVE Bioreactors, GE Healthcare) that was programmed to oscillate at a 3° angle and a speed of 10 rpm. This setup was maintained for a period of up to 10 days, ensuring a constant temperature of 37°C and a CO_2 concentration of 5%. Throughout the rocking motion, the culture medium fully submerged the entire sensor system, enabling optimal conditions for cell growth and evaluation. The stability and continuous operation of the electrochemical sensor were assessed. Consequently, no changes were made to the medium to solely observe the performance of the electrochemical sensors during stem cell proliferation. The C2C12 growth medium was prepared by blending DMEM (Gibco) with 10% FBS (Gibco) and 1% PS (Gibco). Similarly, the mMSC growth medium was formulated by combining DMEM with 10% FBS and 1% PS. Furthermore, the hMSCs were cultured using mesenchymal stem cell basal medium for growth (MSCBM; Lonza).

Preparation of human iPSCs and mPMs in cell culture plates

Human iPSCs were procured from STEMCELL Technologies (Vancouver, BC, Canada). In this study, iPSCs at passage 5 were cultured

on a Matrigel-coated 150-mm tissue culture dish in 70 ml of mTeSR Plus medium. After achieving full attachment within 1 day, biosensors were installed to monitor various parameters. Medium exchange occurred every 2 days until compact colonies and/or enlarged areas reached ~80% confluency. For control samples, iPSCs were cultured similarly without the installation of biosensors. The morphologies of iPSCs were identified through observation using the ECHO Revolve Microscope Generation 2 (A BICO COMPANY, San Diego, CA, USA). mPMs were isolated from Pax7/TdTomato mice (3.06 months old) using a pre-plating method. Two mice were euthanized to isolate mPMs separately; one mouse was designated for biosensor installation, and the other served as a control. For each mouse, muscles from both hind limbs were dissected and collected in PBS. After removing visible fat, nerve deposits, and tendons, the muscles were minced on a sterilized plastic plate using surgical scissors, creating a paste. The paste was digested with 5 ml of 0.2% type II collagenase (LS004177, Worthington Biochemical, Freehold, NJ, USA) prepared in DMEM. After incubating for 60 min at 37°C, a 20-gauge syringe needle was used to mix the digested muscle solution, followed by the addition of 40 ml of DPBS. The minced muscle suspension was then filtered through a 40-μm nylon mesh strainer, and the cell pellet obtained after centrifugation was resuspended in 10 ml of growth medium (DMEM, 20% FBS, and 1% PS). The cell-containing growth medium was incubated in a collagen-coated 100-mm dish for 16 hours and then transferred to another collagen-coated 100-mm dish. After 3 hours, the cell-containing growth medium was moved to a Matrigel-coated 100-mm dish, and basic fibroblast growth factor (bFGF; 10 ng/ml) was added. After 24 hours, the medium with debris was discarded, and fresh growth medium supplemented with bFGF (10 ng/ml) was replaced. After the next 24 hours, the attached cells were trypsinized, centrifuged, and resuspended in 10 ml of fresh growth medium containing bFGF (10 ng/ml). This cell-containing growth medium was incubated in a collagen-coated dish for 5 min, gently shaken to suspend unattached cells, and the incubate-and-shake step was repeated five times. The solution was then moved to a Matrigel-coated 150-mm dish, and 60 ml of bFGF-containing growth medium was added. After a day for cell attachment, biosensors were installed after exchanging the fresh growth medium containing bFGF (10 ng/ml). For the control samples, mPMs from the second mouse were used without biosensor installation, and all steps were kept the same. After 2 days of culture, the cells were switched to differentiation medium (DMEM, 2% horse serum, and 1% PS), and the differentiation medium was exchanged after 2 days. The morphologies of mPMs and myotubes were identified through observation using the ECHO Revolve Microscope Generation 2 (A BICO COMPANY, San Diego, CA, USA).

Preparation of cell-laden hydrogels

The hydrogels encapsulating target cells were fabricated using gelatin-hydroxyphenyl propionic acid (GH) with a phenol content of 144 μmol/g. The enzymatic reaction underwent in the presence of peroxidase from HRP (type VI, 250 to 330 U/mg) and H_2O_2 (Sigma-Aldrich, St. Louis, MO, USA). The hydrogel stiffness was determined by Rheometer (MCR 302e, Anton Paar USA Inc., Houston, TX, USA) in oscillation mode (cone plate, 1% of strain, and angular frequency of 5 rad/s). C2C12 myoblasts (passage 9), mouse bone marrow–derived mMSCs (isolated from femur of C57BL/6 mice), and hMSCs (passage 4, Lonza) were selected as a cell source for the experiments. The cells were homogeneously mixed with gelatin-hydroxyphenyl propionic acid (GH; 5.0 wt %) at a density of 106 cells/ml. In microtube A, the GH/cell mixture (90 μl) and H_2O_2 solution (10 μl, 0.09%) were gently vortexed. In microtube B, GH/cell mixture (90 μl) and HRP solution (10 μl, 0.015 mg/ml) were prepared separately. To form the cell-laden GH hydrogels, solution A and solution B were mixed and added to the PDMS (Corning Sylgard 184) mold. After gel formation for 15 min, the GH/cell hydrogel cubes, having 3.0×10^5 cells per cube, were transferred to the sterilized cell bag containing 1 liter of the cell culture medium. For GH/C2C12 hydrogels, growth media were prepared from DMEM containing 10% FBS and 1% PS. For GH/hMSC hydrogels, growth media were prepared by mixing MSCBM Basal Media (PT-3238, Lonza) and the MSCGM SingleQuots Supplement Kit (PT-4105, Lonza).

Characterization of cultured cells

The method for monitoring various aspects of cell culture, including cell viability, live/dead cell ratio, cellular morphology, and protein content, is described, providing valuable insights into the cellular behavior and overall culture quality. Cell morphology observation was performed with optical microscopy (Axioscope 5, Zeiss). Cells were seeded with 5×10^5 cells per dish in the desired culture plate with 100 mm in a diameter and incubated in 5% CO_2 and 37°C. After cell seeding, the cell morphology was monitored, and images are obtained daily. The GH/cell hydrogels after culturing in cell bags were stained with a LIVE/DEAD viability/cytotoxicity kit to assess the cell viability. To quantify the live cells, a CCK-8 (ALX-850-039-KI01, Enzo Life Sciences Inc., Farmingdale, NY, USA) was performed according to the manufacturer's instruction. In addition, some of GH/cell hydrogels were also stained with Phalloidin-iFluor 647 (ab176750) and with Hoechst 33342, trihydrochloride, trihydrate (10 mg/ml) solution to observe the cell morphology. For the CCK-8 assay, each GH/hMSC hydrogels were incubated in the mixture containing 900 μl of cell culture medium and 100 μl of CCK-8 reagent for 2 hours in the incubator. The OD was determined by a microplate reader at 450 nm, and the cell viability was calculated on the basis of the absorbance values. For live and dead staining, the GH/hMSC hydrogels were washed twice in DPBS. The samples were then immersed in 800 μl of DPBS containing 0.8 μl of calcein-AM and 1.6 μl of EthD-1 for 1 hour. After staining, the samples were washed with DPBS three times and observed by an ECHO Revolve microscope (BICO company, San Diego, CA, USA) in a fluorescent mode (excitation and emission wavelengths of 528/617 nm and 495/515 nm, respectively). In the case of phalloidin and Hoechst staining, the GH/hMSC hydrogels were fixed with 4% paraformaldehyde at room temperature overnight. These samples were then washed with DPBS at least three times. A blocking solution (2% bovine serum albumin, 0.5% goat serum, and 0.5% Triton X-100 in DPBS) of 1 ml containing 1 μl of Phalloidin-iFluor 647 was added to each sample. After the cell fixation, the samples were washed with DPBS twice for 1 hour each and immersed in 1 ml of DPBS containing 10 μl of Hoechst for 1 hour. After washing with DPBS overnight, these stained GH/hMSC hydrogels were observed by a confocal microscope (Model DMi8 automated, Leica Microsystems CMS GmbH, Mannheim, Germany) to produce *Z*-stack images of the whole-sample structure in the view of the field.

Supplementary Materials

This PDF file includes:

Figs. S1 to S33

Tables S1 to S8
Legends for movies S1 to S3

Other Supplementary Material for this manuscript includes the following:
Movies S1 to S3

REFERENCES AND NOTES

1. L. Bagno, K. E. Hatzistergos, W. Balkan, J. M. Hare, Mesenchymal stem cell-based therapy for cardiovascular disease: Progress and challenges. *Mol. Ther.* **26**, 1610–1623 (2018).
2. M. Mimeault, R. Hauke, S. K. Batra, Stem cells: A revolution in therapeutics—Recent advances in stem cell biology and their therapeutic applications in regenerative medicine and cancer therapies. *CPT* **82**, 252–264 (2007).
3. B. A. Syed, J. B. Evans, Stem cell therapy market. *Nat. Rev. Drug Discov.* **12**, 185–186 (2013).
4. V. Volarevic, B. S. Markovic, M. Gazdic, A. Volarevic, N. Jovicic, N. Arsenijevic, L. Armstrong, V. Djonov, M. Lako, M. Stojkovic, Ethical and safety issues of stem cell-based therapy. *Int. J. Med. Sci.* **15**, 36–45 (2018).
5. V. Jossen, C. van den Bos, R. Eibl, D. Eibl, Manufacturing human mesenchymal stem cells at clinical scale: Process and regulatory challenges. *Appl. Microbiol. Biotechnol.* **102**, 3981–3994 (2018).
6. S. Badenes, A. Fernandes-Platzgummer, C. Rodrigues, M. Diogo, C. Da Silva, J. Cabral, "Microcarrier culture systems for stem cell manufacturing" in *Stem Cell Manufacturing* (Elsevier, 2016), pp. 77–104.
7. A. Nienow, K. Coopman, T. Heathman, Q. Rafiq, C. Hewitt, "Bioreactor engineering fundamentals for stem cell manufacturing" in *Stem Cell Manufacturing* (Elsevier, 2016), pp. 43–75.
8. S. G. Klein, S. M. Alsolami, S. Arossa, G. Ramos-Mandujano, A. J. Parry, A. Steckbauer, C. M. Duarte, M. Li, In situ monitoring reveals cellular environmental instabilities in human pluripotent stem cell culture. *Commun. Biol.* **5**, 119 (2022).
9. S. Prill, M. S. Jaeger, C. Duschl, Long-term microfluidic glucose and lactate monitoring in hepatic cell culture. *Biomicrofluidics* **8**, 034102 (2014).
10. P. M. Misun, J. Rothe, Y. R. F. Schmid, A. Hierlemann, O. Frey, Multi-analyte biosensor interface for real-time monitoring of 3D microtissue spheroids in hanging-drop networks. *Microsyst. Nanoeng.* **2**, 16022 (2016).
11. A. Weltin, J. Kieninger, G. Urban, I. Moser, G. Jobst, M. Wego, R. Ehret, in *SENSORS, 2010 IEEE* (IEEE, 2010), pp. 2113–2116.
12. D. Sticker, M. Rothbauer, J. Ehgartner, C. Steininger, O. Liske, R. Liska, W. Neuhaus, T. Mayr, T. Haraldsson, J. P. Kutter, P. Ertl, Oxygen management at the microscale: A functional biochip material with long-lasting and tunable oxygen scavenging properties for cell culture applications. *ACS Appl. Mater. Interfaces* **11**, 9730–9739 (2019).
13. Refresh cell culture, Refresh cell culture. *Nat. Biomed. Eng.* **5**, 783–784 (2021).
14. N. R. Prabhakar, 2019 nobel prize in physiology or medicine. *Phys. Ther.* **35**, 81–83 (2020).
15. An award to oxygen sensing, An award to oxygen sensing. *Nat. Biomed. Eng.* **3**, 843–844 (2019).
16. F. Liebisch, A. Weltin, J. Marzioch, G. A. Urban, J. Kieninger, Zero-consumption Clark-type microsensor for oxygen monitoring in cell culture and organ-on-chip systems. *Sens. Actuators B* **322**, 128652 (2020).
17. H. J. Choi, T. B. Ngoc, H. Song, C. H. Chang, G. M. Kim, Fabrication of microfluidic cell culture platform for real-time monitoring of lidocaine concentration. *Int. J. Precis. Eng. Manuf. INT J PRECIS ENG MAN* **21**, 2399–2405 (2020).
18. S. G. Klein, S. M. Alsolami, A. Steckbauer, S. Arossa, A. J. Parry, G. Ramos Mandujano, K. Alsayegh, J. C. Izpisua Belmonte, M. Li, C. M. Duarte, A prevalent neglect of environmental control in mammalian cell culture calls for best practices. *Nature. Biomed. Eng.* **5**, 787–792 (2021).
19. J. P. A. Ioannidis, B. Y. S. Kim, A. Trounson, How to design preclinical studies in nanomedicine and cell therapy to maximize the prospects of clinical translation. *Nat. Biomed. Eng.* **2**, 797–809 (2018).
20. Design preclinical studies for reproducibility, Design preclinical studies for reproducibility. *Nat. Biomed. Eng.* **2**, 789–790 (2018).
21. D. Schop, F. Janssen, E. Borgart, J. De Bruijn, R. van Dijkhuizen-Radersma, Expansion of mesenchymal stem cells using a microcarrier-based cultivation system: Growth and metabolism. *J. Tissue Eng. Regen. Med.* **2**, 126–135 (2008).
22. C. J. Hewitt, K. Lee, A. W. Nienow, R. J. Thomas, M. Smith, C. R. Thomas, Expansion of human mesenchymal stem cells on microcarriers. *Biotechnol. Lett.* **33**, 2325–2335 (2011).
23. M. Croughan, D. Giroux, D. Fang, B. Lee, "Novel single-use bioreactors for scale-up of anchorage-dependent cell manufacturing for cell therapies" in *Stem Cell Manufacturing* (Elsevier, 2016), pp. 105–139.
24. J. Lee, M. C. Kim, I. Soltis, S. H. Lee, W.-H. Yeo, Advances in electrochemical sensors for detecting analytes in biofluids. *Advanced Sensor Research* **2**, 2200088 (2023).
25. K. Schneider, V. Schütz, G. T. John, E. Heinzle, Optical device for parallel online measurement of dissolved oxygen and pH in shake flask cultures. *Bioprocess Biosyst. Eng.* **33**, 541–547 (2010).
26. J. N. Warnock, M. Al-Rubeai, Bioreactor systems for the production of biopharmaceuticals from animal cells. *Biotechnol. Appl. Biochem.* **45**, 1–12 (2006).
27. D. C. Kirouac, P. W. Zandstra, The systematic production of cells for cell therapies. *Cell Stem Cell* **3**, 369–381 (2008).
28. F. F. dos Santos, P. Z. Andrade, C. L. da Silva, J. M. Cabral, Bioreactor design for clinical-grade expansion of stem cells. *Biotechnol. J.* **8**, 644–654 (2013).
29. K. W. Cho, S. J. Kim, J. Kim, S. Y. Song, W. H. Lee, L. Wang, M. Soh, N. Lu, T. Hyeon, B.-S. Kim, Large scale and integrated platform for digital mass culture of anchorage dependent cells. *Nat. Commun.* **10**, 1–13 (2019).
30. M. Tric, M. Lederle, L. Neuner, I. Dolgowjasow, P. Wiedemann, S. Wölfl, T. Werner, Optical biosensor optimized for continuous in-line glucose monitoring in animal cell culture. *Anal. Bioanal. Chem.* **409**, 5711–5721 (2017).
31. G. L. Converse, E. E. Buse, K. R. Neill, C. R. McFall, H. N. Lewis, M. C. VeDepo, R. W. Quinn, R. A. Hopkins, Design and efficacy of a single-use bioreactor for heart valve tissue engineering. *J. Biomed. Mater. Res. B Appl. Biomater.* **105**, 249–259 (2017).
32. J. Kieninger, Y. Tamari, B. Enderle, G. Jobst, J. A. Sandvik, E. O. Pettersen, G. A. Urban, Sensor access to the cellular microenvironment using the sensing cell culture flask. *Biosensors* **8**, 44 (2018).
33. T. Nguyen, S. Cho, V. Bhola, S. Ko, R. Sharma, J. Magda, P. Tathireddy, in *2015 Transducers-2015 18th International Conference on Solid-State Sensors, Actuators and Microsystems (TRANSDUCERS)* (IEEE, 2015), pp. 1684–1687.
34. S. Udomsom, A. Budwong, C. Wongsa, P. Sangngam, P. Baipaywad, C. Manaspon, S. Auephanwiriyakul, N. Theera-Umpon, P. Paengnakorn, Automatic programmable bioreactor with pH monitoring system for tissue engineering application. *Bioengineering* **9**, 187 (2022).
35. J. Marzioch, J. Kieninger, A. Weltin, H. Flamm, K. Aravindalochanan, J. A. Sandvik, E. O. Pettersen, Q. Peng, G. A. Urban, On-chip photodynamic therapy – Monitoring cell metabolism using electrochemical microsensors. *Lab Chip* **18**, 3353–3360 (2018).
36. J. M. Stine, L. A. Beardslee, R. M. Sathyam, W. E. Bentley, R. Ghodssi, Electrochemical dissolved oxygen sensor-integrated platform for wireless in situ bioprocess monitoring. *Sens. Actuators B* **320**, 128381 (2020).
37. Y. Lee, C. Howe, S. Mishra, D. S. Lee, M. Mahmood, M. Piper, Y. Kim, K. Tieu, H.-S. Byun, J. P. Coffey, Wireless, intraoral hybrid electronics for real-time quantification of sodium intake toward hypertension management. *Proc. Natl. Acad. Sci.* **115**, 5377–5382 (2018).
38. H.-R. Lim, N. Hillman, Y.-T. Kwon, Y.-S. Kim, Y.-H. Choa, W.-H. Yeo, Ultrathin, long-term stable, solid-state reference electrode enabled by enhanced interfacial adhesion and conformal coating of AgCl. *Sens. Actuators B* **309**, 127761 (2020).
39. H.-R. Lim, S. M. Lee, S. Park, C. Choi, H. Kim, J. Kim, M. Mahmood, Y. Lee, J.-H. Kim, W.-H. Yeo, Smart bioelectronic pacifier for real-time continuous monitoring of salivary electrolytes. *Biosens. Bioelectron.* **210**, 114329 (2022).
40. H. E. Amor, A. B. Kouki, P. Marsh, K. T. Kim, H. Cao, in *2016 IEEE SENSORS* (IEEE, 2016), pp. 1–3.
41. W.-D. Huang, H. Cao, S. Deb, M. Chiao, J.-C. Chiao, A flexible pH sensor based on the iridium oxide sensing film. *Sens. Actuator A Phys.* **169**, 1–11 (2011).
42. H. Jia, G. Chang, H. Shu, M. Xu, X. Wang, Z. Zhang, X. Liu, H. He, K. Wang, R. Zhu, Pt nanoparticles modified Au dendritic nanostructures: Facile synthesis and enhanced electrocatalytic performance for methanol oxidation. *Int. J. Hydrogen Energy* **42**, 22100–22107 (2017).
43. W. Xie, F. Zhang, Z. Wang, M. Yang, J. Xia, R. Gui, Y. Xia, Facile preparation of PtPdPt/graphene nanocomposites with ultrahigh electrocatalytic performance for methanol oxidation. *J. Electroanal. Chem.* **761**, 55–61 (2016).
44. T. Xia, J. Liu, S. Wang, C. Wang, Y. Sun, L. Gu, R. Wang, Enhanced catalytic activities of NiPt truncated octahedral nanoparticles toward ethylene glycol oxidation and oxygen reduction in alkaline electrolyte. *ACS Appl. Mater. Interfaces* **8**, 10841–10849 (2016).
45. H. Kudo, T. Sawada, M. X. Chu, T. Saito, H. Saito, K. Otsuka, Y. Iwasaki, K. Mitsubayashi, in *SENSORS, 2006 IEEE* (IEEE, 2006), pp. 620–623.
46. G. Sposito, *The Environmental Chemistry of Aluminum* (CRC Press, 2020).
47. A. Teo, A. Mantalaris, M. Lim, Influence of culture pH on proliferation and cardiac differentiation of murine embryonic stem cells. *Biochem. Eng. J.* **90**, 8–15 (2014).
48. J. Michl, K. C. Park, P. Swietach, Evidence-based guidelines for controlling pH in mammalian live-cell culture systems. *Commun. Biol.* **2**, 144 (2019).
49. W. Y. Du, *Resistive, Capacitive, Inductive, and Magnetic Sensor Technologies* (CRC Press, 2014).
50. J. H. Anderson, *Measurement of Thermal Conductivity of Gold Nanofilms and Nanowires* (Texas State University, 2020).
51. V. A. Sandborn, *Resistance Temperature Transducers* (Metrology Press, 1972).
52. P. Zimmermann, A. Weltin, G. A. Urban, J. Kieninger, Active potentiometry for dissolved oxygen monitoring with platinum electrodes. *Sensors* **18**, 2404 (2018).
53. S. A. Mousavi Shaegh, F. De Ferrari, Y. S. Zhang, M. Nabavinia, N. Binth Mohammad, J. Ryan, A. Pourmand, E. Laukaitis, R. Banan Sadeghian, A. Nadhman, A microfluidic optical platform for real-time monitoring of pH and oxygen in microfluidic bioreactors and organ-on-chip devices. *Biomicrofluidics* **10**, 044111 (2016).

54. B. R. Weil, A. M. Abarbanell, J. L. Herrmann, Y. Wang, D. R. Meldrum, High glucose concentration in cell culture medium does not acutely affect human mesenchymal stem cell growth factor production or proliferation. *Am. J. Physiol. Regul.* **296**, R1735–R1743 (2009).
55. N. Saki, M. A. Jalalifar, M. Soleimani, S. Hajizamani, F. Rahim, Adverse effect of high glucose concentration on stem cell therapy. *IJHOSCR* **7**, 34–40 (2013).
56. Y. Lee, B. Nicholls, D. Sup Lee, Y. Chen, Y. Chun, C. Siang Ang, W.-H. Yeo, Soft electronics enabled ergonomic human-computer interaction for swallowing training. *Sci. Rep.* **7**, 1–12 (2017).
57. Y.-T. Kwon, H. Kim, M. Mahmood, Y.-S. Kim, C. Demolder, W.-H. Yeo, Printed, wireless, soft bioelectronics and deep learning algorithm for smart human–machine interfaces. *ACS Appl. Mater. Interfaces* **12**, 49398–49406 (2020).
58. S. R. Caliari, J. A. Burdick, A practical guide to hydrogels for cell culture. *Nat. Methods* **13**, 405–414 (2016).
59. C. Jensen, Y. Teng, Is it time to start transitioning from 2D to 3D cell culture? *Front. Mol. Biosci.* **7**, 33 (2020).
60. A. Fedi, C. Vitale, P. Giannoni, G. Caluori, A. Marrella, Biosensors to monitor cell activity in 3D hydrogel-based tissue models. *Sensors* **22**, 1517 (2022).
61. S.-M. Lee, N. Han, R. Lee, I.-H. Choi, Y.-B. Park, J.-S. Shin, K.-H. Yoo, Real-time monitoring of 3D cell culture using a 3D capacitance biosensor. *Biosens. Bioelectron.* **77**, 56–61 (2016).
62. R. Edmondson, J. J. Broglie, A. F. Adcock, L. Yang, Three-dimensional cell culture systems and their applications in drug discovery and cell-based biosensors. *Assay Drug Dev. Technol.* **12**, 207–218 (2014).
63. E. Gantumur, S. Sakai, M. Nakahata, M. Taya, Horseradish peroxidase-catalyzed hydrogelation consuming enzyme-produced hydrogen peroxide in the presence of reducing sugars. *Soft Matter* **15**, 2163–2169 (2019).
64. S. H. Lee, Y. Lee, Y. W. Chun, S. W. Crowder, P. P. Young, K. D. Park, H.-J. Sung, In situ crosslinkable gelatin hydrogels for vasculogenic induction and delivery of mesenchymal stem cells. *Adv. Funct. Mater.* **24**, 6771–6781 (2014).
65. Y. Lee, J. W. Bae, J. W. Lee, W. Suh, K. D. Park, Enzyme-catalyzed in situ forming gelatin hydrogels as bioactive wound dressings: Effects of fibroblast delivery on wound healing efficacy. *J. Mater. Chem. B* **2**, 7712–7718 (2014).
66. Composition and mechanism of three-dimensional hydrogel system in regulating stem cell fate. *Tissue Eng. Part B Rev.* **26**, 498–518 (2020).
67. C. W. Kim, C. J. Kim, E. H. Park, S. Ryu, Y. Lee, E. Kim, K. Kang, K. Y. Lee, E. H. Choo, B. H. Hwang, H. J. Youn, K. D. Park, K. Chang, MSC-encapsulating in situ cross-linkable gelatin hydrogels to promote myocardial repair. *ACS Appl. Bio Mater.* **3**, 1646–1655 (2020).
68. S. P. Medvedev, A. I. Shevchenko, S. M. Zakian, Induced pluripotent stem cells: Problems and advantages when applying them in regenerative medicine. *Acta Naturae* **2**, 18–27 (2010).
69. M. Scudellari, How iPS cells changed the world. *Nature* **534**, 310–312 (2016).
70. R. Castro-Vinuelas, C. Sanjurjo-Rodriguez, M. Pineiro-Ramil, S. Rodriguez-Fernandez, I. Lopez-Baltar, I. Fuentes-Boquete, F. J. Blanco, S. Diaz-Prado, Tips and tricks for successfully culturing and adapting human induced pluripotent stem cells. *Mol. Ther. Methods Clin. Dev.* **23**, 569–581 (2021).
71. M. Rivas, "Iridium oxide (IrO2) as a top electrode for ferroelectric micro-electro-mechanical systems (MEMS) devices for radiation rich environments," thesis, University of Connecticut, Storrs, CT (2018).
72. H. Huang, F. Spaepen, Tensile testing of free-standing Cu, Ag and Al thin films and Ag/Cu multilayers. *Acta Mater.* **48**, 3261–3269 (2000).
73. X. Zhang, H. Hao, Y. Shi, J. Cui, The mechanical properties of Polyvinyl Butyral (PVB) at high strain rates. *Construct. Build Mater.* **93**, 404–415 (2015).
74. W. Kirsten, A. Krüger, H. W. J. P. Neomagus, D. G. Bessarabov, Effect of relative humidity and temperature on the mechanical properties of PFSA Nafion-cation-exchanged membranes for electrochemical applications. *Int. J. Electrochem. Sci.* **12**, 2573–2582 (2017).
75. C. Christian, B. Amine, P. Caroline, "Polyvinyl Butyral" in *Handbook of Thermoplastics* (CRC Press, 2015), 89–137.
76. T. Aouak, W. S. Saeed, N. M. Al-Hafi, A.-B. Al-Odayni, A. A. Alghamdi, I. Bedja, Poly (2-hydroxyethylmethacrylate –co–methylmethacrylate)/lignocaine contact lens preparation, characterization, and in vitro release dynamic. *Polymers* **11**, 917 (2019).
77. D. G. Papageorgiou, I. A. Kinloch, R. J. Young, Mechanical properties of graphene and graphene-based nanocomposites. *Prog. Mater. Sci* **90**, 75–127 (2017).
78. G. Cao, Atomistic studies of mechanical properties of graphene. *Polymers* **6**, 2404–2432 (2014).
79. K. W. Cho, S. J. Kim, J. Kim, S. Y. Song, W. H. Lee, L. Wang, M. Soh, N. Lu, T. Hyeon, B.-S. Kim, D.-H. Kim, Large scale and integrated platform for digital mass culture of anchorage dependent cells. *Nat. Commun.* **10**, 4824 (2019).
80. I. Podunavac, T. Knežić, M. Djisalov, N. Omerovic, M. Radovic, L. Janjušević, D. Stefanovic, M. Panic, I. Gadjanski, V. Radonic, Mammalian cell-growth monitoring based on an impedimetric sensor and image processing within a microfluidic platform. *Sensors* **23**, 3748 (2023).
81. C. Wongsa, S. Udomsom, A. Budwong, K. Kiwfo, K. Grudpan, P. Paengnakorn, Sequential injection amperometric system coupling with bioreactor for in-line glucose monitoring in cell culture application. *Molecules* **27**, (2022).
82. S. Kreß, R. Schaller-Ammann, J. Feiel, J. Wegener, J. Priedl, W. Dietrich, C. Kasper, D. Egger, Innovative platform for the advanced online monitoring of three-dimensional cells and tissue cultures. *Cell* **11**, 412 (2022).

Acknowledgments

Funding: This research was supported by funds from the Marcus Foundation, the Georgia Research Alliance, and the Georgia Tech Foundation through the support of the Marcus Center for Therapeutic Cell Characterization and Manufacturing (MC3M) at Georgia Tech. In addition, this work was partially funded by the IEN Center for Wearable Intelligent Systems and Healthcare at Georgia Tech and the NSF Engineering Research Center for Cell Manufacturing Technologies (CMaT; EEC 1648035). **Author contributions:** Conceptualization: J.L., H.-R.L., and W.-H.Y. Methodology: J.L., Hojoong Kim, H.-R.L., Y.S.K., T.T.T.H., J.C., G.-J.J., I.S., K.R.K., Hodam Kim, R.H., S.H.L., Y.K., Y.L., Y.C.J., and W.-H.Y. Investigation: J.L., Hojoong Kim, H.-R.L., Y.S.K., T.T.T.H., J.C., G.-J.J., I.S., K.R.K., Hodam Kim, R.H., S.H.L., Y.K., Y.L., Y.C.J., and W.-H.Y. Visualization: J.L., H.-R.L., Y.S.K., T.T.T.H., R.H., S.H.L., Y.K., and Y.L. Supervision: Y.C.J. and W.-H.Y. Writing—original draft: J.L., Hojoong Kim, and T.T.T.H. Writing—review and editing: J.L., Hojoong Kim, T.T.T.H., Y.L., Y.C.J., and W.-H.Y. **Competing interests:** W.-H.Y., Y.S.K., and J.L. are inventors on a pending patent application related to this work. The authors declare that they have no other competing interests. **Data and materials availability:** All data needed to evaluate the conclusions in the paper are present in the paper and/or the Supplementary Materials.

Submitted 4 September 2023
Accepted 17 January 2024
Published 14 February 2024
10.1126/sciadv.adk6714